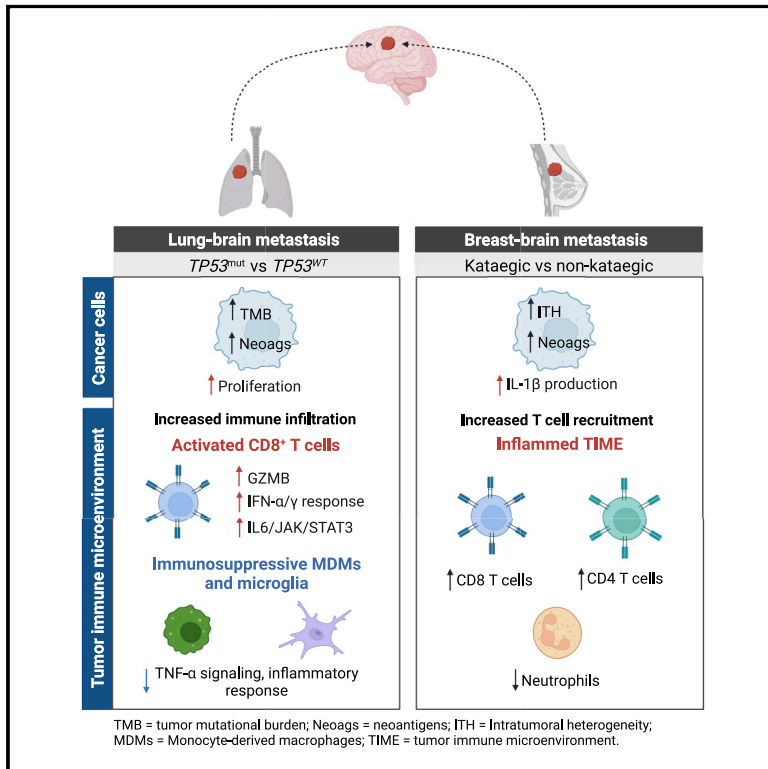


Immunogenomic analysis of human brain metastases reveals diverse immune landscapes across genetically distinct tumors

Graphical abstract



Authors

Ángel F. Álvarez-Prado, Roeltje R. Maas, Klara Soukup, ..., Roy T. Daniel, Monika E. Hegi, Johanna A. Joyce

Correspondence

johanna.joyce@unil.ch

In brief

Álvarez-Prado et al. report a multiparametric immunogenomic analysis of human lung- and breast-to-brain metastases revealing diverse tumor immune microenvironment compositions and phenotypes across genetically distinct tumors.

Highlights

- *TP53^{mut}* shows higher immune cell infiltration than *TP53^{WT}* lung-BrMs
- *TP53^{mut}* lung-BrMs show more activated CD8 T cells and more immunosuppressive TAMs
- Focalized hypermutation (kataegis) occurs in 44% of the analyzed breast-BrMs
- Kataegic breast-BrMs present a higher proportion of T cells and a more inflamed TIME



Article

Immunogenomic analysis of human brain metastases reveals diverse immune landscapes across genetically distinct tumors

Ángel F. Álvarez-Prado,^{1,2,3,4} Roeltje R. Maas,^{1,2,3,4,5,6,10} Klara Soukup,^{1,2,3,10} Florian Klemm,^{1,2,3} Mara Kornete,^{1,2,3} Fanny S. Krebs,^{1,7} Vincent Zoete,^{1,7} Sabina Berezowska,⁸ Jean-Philippe Brouland,⁸ Andreas F. Hottinger,^{1,4,9} Roy T. Daniel,^{4,6} Monika E. Hegi,^{4,5,6} and Johanna A. Joyce^{1,2,3,4,11,*}

¹Department of Oncology, University of Lausanne, 1011 Lausanne, Switzerland

²Ludwig Institute for Cancer Research, University of Lausanne, 1011 Lausanne, Switzerland

³Agora Cancer Research Center, 1011 Lausanne, Switzerland

⁴L. Lundin and Family Brain Tumor Research Center, Departments of Oncology and Clinical Neurosciences, Centre Hospitalier Universitaire Vaudois, 1011 Lausanne, Switzerland

⁵Neuroscience Research Center, Centre Hospitalier Universitaire Vaudois, Lausanne, Switzerland

⁶Department of Neurosurgery, Centre Hospitalier Universitaire Vaudois, Lausanne, Switzerland

⁷Swiss Institute of Bioinformatics, Lausanne, Switzerland

⁸Department of Pathology, Centre Hospitalier Universitaire Vaudois, Lausanne, Switzerland

⁹Brain and Spine Tumor Center, Departments of Clinical Neurosciences and Oncology, Centre Hospitalier Universitaire Vaudois, Lausanne, Switzerland

¹⁰These authors contributed equally

¹¹Lead contact

*Correspondence: johanna.joyce@unil.ch

<https://doi.org/10.1016/j.xcrm.2022.100900>

SUMMARY

Brain metastases (BrMs) are the most common form of brain tumors in adults and frequently originate from lung and breast primary cancers. BrMs are associated with high mortality, emphasizing the need for more effective therapies. Genetic profiling of primary tumors is increasingly used as part of the effort to guide targeted therapies against BrMs, and immune-based strategies for the treatment of metastatic cancer are gaining momentum. However, the tumor immune microenvironment (TIME) of BrM is extremely heterogeneous, and whether specific genetic profiles are associated with distinct immune states remains unknown. Here, we perform an extensive characterization of the immunogenomic landscape of human BrMs by combining whole-exome/whole-genome sequencing, RNA sequencing of immune cell populations, flow cytometry, immunofluorescence staining, and tissue imaging analyses. This revealed unique TIME phenotypes in genetically distinct lung- and breast-BrMs, thereby enabling the development of personalized immunotherapies tailored by the genetic makeup of the tumors.

INTRODUCTION

Advanced metastatic disease is associated with poor treatment efficacy and is a major cause of patient mortality. Brain metastases (BrMs) are the most common form of brain cancer in adults, originating frequently from lung (40%–50%) and breast (15%–25%) primary tumors.^{1,2} BrM results in progressive neurologic disability and impairment of key cognitive and motor functions that severely decrease the quality of life for patients. Furthermore, cancer patients with BrM face a dismal prognosis, with a median overall survival post-BrM detection of 7 and 9 months for lung- and breast-BrMs, respectively.³ Currently available treatments are largely palliative,^{3,4} and effective therapies for BrM disease thus represent an urgent clinical need. In this regard, the therapeutic repertoire targeted against BrM has been expanded from the traditional whole-brain radiotherapy and surgery to

include more precise stereotactic radiosurgery approaches, molecularly targeted therapies, and immunotherapies.⁴

The genetic profile of primary tumors has been recently integrated with prognostic scores, with the objective of guiding treatment decisions for lung- and melanoma-BrM patients.³ This now includes assessing the mutational status for *EGFR/ALK* in lung,⁵ and *BRAF* in melanoma,⁶ as key clinical parameters. Moreover, immune checkpoint blockade (ICB) has shown promising initial outcomes in certain patients with lung- or melanoma-BrM, and several clinical trials are currently ongoing for BrMs originating from breast and other primary cancers.⁴ A phase II trial evaluating the anti-PD1 antibody pembrolizumab demonstrated response rates of 29.7% and 22% in patients with brain-metastatic lung and melanoma cancers, respectively.^{7,8} Other clinical studies combining anti-CTLA4 (ipilimumab) and anti-PD-1 (nivolumab) antibody treatment have



reported intracranial response rates between 45% and 60% in melanoma-BrM patients.^{9–11} Despite these encouraging results, a substantial proportion of BrMs overall remain unresponsive to immunotherapy, likely reflecting the underlying complexity and heterogeneity of the BrM tumor immune microenvironment (TIME)^{12–14} and the necessity for a comprehensive and integrated understanding of the factors driving pro- or anti-tumoral roles for the immune system in these patients.

Multiparametric analysis of large collections of primary and metastatic brain tumors has revealed that BrMs present characteristic TIMEs, which are shaped by the tumor of origin and are distinct from the TIME of gliomas.^{15,16} In addition, recent single-cell integrative analyses of BrMs identified two distinct and co-existing functional BrM archetypes (“proliferative” and “inflammatory”), which are consistent with previously identified states in metastases to other organs and defined by tumor-immune interactions.¹⁷ The importance of the TIME in regulating tumor progression, metastatic dissemination, and response to immunotherapy has been reported for several primary cancers.^{18–23} Likewise, a correlation between the genetic makeup of a tumor and its TIME composition and phenotype was described for pancreatic cancer²⁴ and primary pediatric²⁵ and adult^{15,26} brain tumors.

Although extensive genomic profiling of primary and metastatic tumors has been performed to identify genetic determinants of metastatic disease in patients,^{13,27–32} whether the immune landscape of these tumors is influenced by their underlying genetic makeup currently remains unknown. Therefore, to address this critical question, we performed a comprehensive immunogenomic analysis of lung- and breast-BrMs by combining whole-exome and whole-genome sequencing of tumors, RNA sequencing of purified immune populations (encompassing >170 transcriptomes), flow cytometry, and immunofluorescence analyses. Our data revealed that specific genetic drivers correlate with distinct immune landscapes in BrMs, with *TP53*-mutant lung-BrMs presenting with an increased CD8⁺ T cell infiltration and activation, but a more immunosuppressive myeloid compartment, and hypermutated breast-BrMs showing a generally more pro-inflammatory microenvironment. These results support the incorporation of genetic profiling of BrMs as a means to potentially predict responses to current immunotherapies and for the development of personalized immune-based interventions informed by the genetic makeup of the tumors.

RESULTS

The genomic landscape of lung- and breast-to-brain metastatic tumors

We collected surgically resected tissue and matched peripheral blood, as germline controls, from 30 patients with pathologically confirmed BrM tumors, with 21 originating from lung and nine from breast primary cancers (Figure 1A, Table S1A). Tumor samples were processed immediately following surgical resection and were subjected to multiparametric immunogenomic profiling including whole-exome/low-pass whole-genome sequencing (WES/LP-WGS), RNA sequencing (RNA-seq) of sorted populations, flow cytometry (FCM), and immunofluorescence (IF) tissue staining analyses (“Immunogenomics cohort,” Figure 1A, left), using a previously described comprehensive experimental pipeline.³³ In addition, we analyzed an independently collected “validation cohort” of 18 frozen tumor tissue and matched paired peripheral blood mononuclear cell (PBMC) samples, with five originating from lung and 13 from breast primary tumors (Figure 1A, right; Table S1B), which were subjected to WES, RNA-seq of bulk tissue, and IF staining.

We performed WES at an average depth of 170× on matched BrM tumor and PBMC samples and detected a total of 9,349 non-synonymous variants in the immunogenomics cohort (Table S2), encompassing single-nucleotide variants (SNVs) and short insertions and deletions (INDELS). We observed varying degrees of overall mutational load in the different lung-BrMs (Figure 1B, top panel), which did not correlate with chemotherapy or radiotherapy treatment, as evidenced by the presence of treatment-naïve samples among the most mutated and treated samples among the least mutated (non-synonymous mutations treated vs. untreated, unpaired two-tailed t test, $p > 0.05$ for both chemotherapy and radiotherapy; Figure 1B, Tables S1 and S2), nor with dexamethasone treatment (non-synonymous mutations treated vs. untreated, unpaired two-tailed t test, $p > 0.05$, Figure 1B, Tables S1 and S2). When compared with the average tumor mutational burden (TMB) of 33 different primary cancer types from The Cancer Genome Atlas (TCGA), our lung-BrM cohort showed a similar, yet slightly higher, mutational load compared with lung primary tumors (Figure 1C), which is in agreement with the branched evolution model reported for tumors that metastasize to the brain.²⁷

Figure 1. The genomic landscape of lung-to-brain metastases

- (A) Schematic overview of the study. BrM, brain metastasis; PBMC, peripheral blood mononuclear cells; WES, whole-exome sequencing; LP-WGS, low-pass whole-genome sequencing; RNA-seq, RNA sequencing; IF, immunofluorescence; CD45-neg, CD45-negative cells; MDM, monocyte-derived macrophages.
- (B) Oncoplot summarizing genomic features of lung-BrMs in the immunogenomics cohort ($n = 21$, in red), including mutational load (upper panel), mutations (central panel), and mutation prevalence (central left panel) of mutated lung cancer drivers; copy number variation (CNV) status of selected genes (second central panel, only CNV alterations identified by both WES and LP-WGS are reported here); summary of individual nucleotide changes in all mutated genes (third central panel); mutational signatures (fourth central panel) and clinical information, including time from the end of the last chemo/radio/immunotherapy treatment prior to surgical resection of the BrM (i.e., > 6 months indicates that the corresponding treatment was finished more than 6 months before surgery), duration of dexamethasone treatment, sex, and histological subtype of the primary tumor (bottom panels). Radiation treatment modality corresponds to stereotactic radiosurgery (SRS) in all radiotherapy-treated samples.
- (C) Comparison of tumor mutational burden (TMB) between lung-BrM samples in this study ($n = 21$) and 33 primary cancer types from The Cancer Genome Atlas (TCGA). Each dot represents the mutational burden of one tumor; total number of tumors per primary cancer is indicated above the plot.
- (D) Total number of mutations in lung-BrMs ($TP53^{mut} n = 9$; $TP53^{mut}KRAS^{mut} n = 5$; $KRAS^{mut} n = 2$; NP/NK $n = 5$ biological replicates; one-way ANOVA test $p = 0.0002$; Dunnett’s multiple comparisons test **adjusted $p < 0.01$, ****adjusted $p < 0.0001$).
- (E) Total number of neoantigens in lung-BrMs ($TP53^{mut} n = 9$; $TP53^{mut}KRAS^{mut} n = 5$; $KRAS^{mut} n = 2$; NP/NK $n = 5$ biological replicates; ANOVA/Kruskal-Wallis test $p = 0.025$; Dunn’s multiple comparisons test *adjusted $p < 0.05$, ***adjusted $p < 0.001$). See also Tables S1–S5.

We identified *TP53* and *KRAS* as the two most prevalently mutated lung cancer driver genes in our lung-BrM cohort (Figure 1B, left panel; Tables S2 and S3). This is consistent with recently published collections of lung-BrMs: *TP53* and *KRAS* mutations were observed in 64% and 32% of lung-BrMs, respectively, in our immunogenomics cohort (n = 21) vs. 64% and 40% in the Brastianos cohort (n = 73),³¹ 63% and 61% in the Berezowska cohort (n = 57),³² and 60% and 40% in the Dunn cohort (n = 6).¹³ Moreover, this comparison indicates that the number of samples included in this immunogenomics study is adequate to provide an accurate representation of the genetic heterogeneity of lung-BrMs. While most of the SNVs identified in *TP53* correspond to nonsense mutations or frameshift INDELS, missense mutations were also detected (Figure 1B, central panel). To assess the functional relevance of these mutations, we analyzed their prevalence in primary lung tumors from the TCGA and their predicted “driver” or “passenger” status as defined by *in silico* mutagenesis analysis (Figure S1A³⁴). Interestingly, all missense mutations identified in lung-BrMs are frequently found in primary lung cancers and predicted to be cancer drivers (Figure S1A, red arrows). We further assessed the structural impact of these missense SNVs by computing the differential in Gibbs free energy between the mutant and wild-type forms and found them to be destabilizing for P53 binding to DNA (Figure S1B). In addition, several of these mutations occurred in well-conserved amino acid residues, suggesting that they are functionally relevant (Figure S1C). Together, these results support a loss-of-function role for the *TP53* missense mutations identified herein in lung-BrMs. For *KRAS*, by contrast, most SNVs that we identified correspond to well-known gain-of-function mutations including G12C, G13D, and G12V (Figure 1B, central panel³⁵), representing the most frequent *KRAS* mutations in lung adenocarcinomas.³⁶

In order to identify other potential driver genes, we looked for evidence of positive selection on SNVs in our lung-BrM cohort by using the well-established dNdScv algorithm.³⁷ We recovered just two significant hits, *TP53* (adjusted p = 8.9e-12) and *KRAS* (adjusted p = 1.3e-5), consistent with the analyses above. This was further validated by an alternative driver detection method based on the detection of genomic regions with somatic mutation clustering signals (OncoDriveCLUSTL³⁸). Given the emerging relevance of co-occurring genomic alterations mediating diverse phenotypes in primary lung cancers,³⁹ we next evaluated the co-occurrence and co-exclusion of *TP53* and *KRAS* SNVs with mutations in other genes (Figure S2). No significant hits were detected for *KRAS*, whereas *TP53* mutations significantly co-occurred with mutations in very large genes,

including *TTN* (300Kb), *USH2A* (800Kb), and *CSMD3* (1.2Mb), which are more susceptible to false positive signals in genomic analyses than average-sized (~10–15Kb) genes. Indeed, none of these genes have been formally ascribed a pro-tumorigenic function *in vivo*, and only *CSMD3* has been tested *in vitro*, where its loss was associated with increased proliferation in airway epithelial cells.⁴⁰ We also characterized the copy number variation (CNV) landscape of the tumors by whole-exome and LP-WGS (see STAR Methods for details), and we found known drivers of metastatic lung cancer, including amplifications in *MYC*, *YAP*, and *MMP13* and deletions in *CDKN2A/B* loci (Figures 1B, S3A, and S3B³¹).

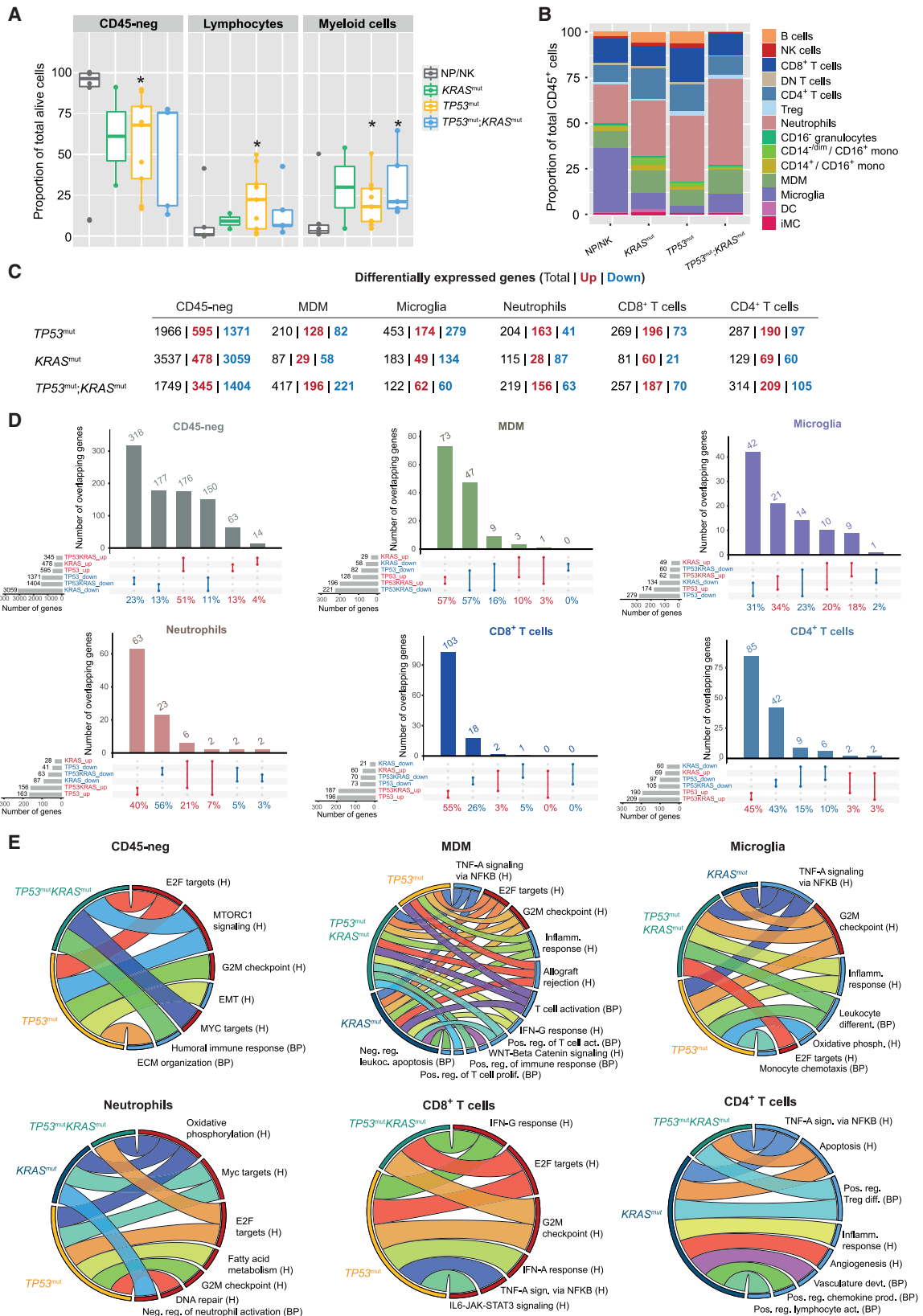
Finally, we interrogated the individual nucleotide changes occurring in each of the tumors and performed mutational signature deconvolution analysis (Figures 1B and S4^{41–43}). Signature 4, associated with tobacco smoking and transcription-coupled nucleotide repair of bulky DNA adducts, dominated the mutational spectrum of most lung-BrMs, followed by signature 5 (clock-like, of unknown etiology but increased in many cancers by tobacco smoking) and signature 2 (attributed to the mutational activity of AID/APOBEC deaminases).^{41–43} These results indicate that lung-BrMs retain the mutational footprint of the primary tumor of origin.

In light of these data, we segregated our lung-BrM cohort into four genetically distinct groups: *TP53* mutant (*TP53*^{mut}, n = 9), both *TP53* and *KRAS* mutant (*TP53*^{mut};*KRAS*^{mut}, n = 5), *KRAS* mutant (*KRAS*^{mut}, n = 2), and non-*TP53*, non-*KRAS* mutant (NP/NK, n = 5), with the latter being composed of tumors presenting other oncogenic alterations commonly found in primary lung tumors and lung-BrMs, such as amplifications in *MMP13*, *ERBB2*, *EGFR*, and *MET* (Figures S3A and S3B; Tables S4 and S5³⁹); or gene fusions involving *ALK*, *RET* and *ROS1* (Table S6³⁹). We then compared the total mutational load of tumors in each of these groups and found that *TP53*^{mut} and *TP53*^{mut};*KRAS*^{mut} BrMs were significantly more mutated than *KRAS*^{mut} or NP/NK BrMs (Figure 1D). Neoantigen prediction analysis revealed that *TP53*^{mut} and *TP53*^{mut};*KRAS*^{mut} lung-BrMs also displayed a higher number of neoantigens (Figure 1E; Table S7). We further estimated intratumoral heterogeneity (ITH) by measuring clonal and subclonal variants (Figure S5, see STAR Methods for details) and found that a large proportion of *TP53*^{mut} and *TP53*^{mut};*KRAS*^{mut} lung-BrMs (77% and 80% respectively, vs. 50% of *KRAS*^{mut} and NP/NK tumors) present with a high ITH (i.e., >50% subclonal variants, Figures S5A, S5C, and S5D).

A detailed characterization of the genomic landscape of breast-BrM (Figure 2) revealed *TP53* as the most prevalently mutated breast cancer driver gene in this cohort (Figure 2A). We also detected SNV and CNV alterations previously described

Figure 2. The genomic landscape of breast-to-brain metastases

- (A) Oncoplot summarizing genomic features of breast-BrMs (n = 9) in the immunogenomics cohort (panels as in Figure 1B).
 (B) Comparison of TMB between breast-BrMs from this study (n = 9, in red) and 33 primary cancers from the TCGA.
 (C) Rainfall plots of kataeic breast-BrMs. Y axis depicts the distance between consecutive mutations; red arrows indicate genomic regions where kataeic was detected.
 (D) Total number of mutations (left panel) and neoantigens (right panel) in breast-BrMs (kataeic, n = 4; non-kataeic, n = 5 biological replicates; unpaired two-tailed Mann-Whitney test *p < 0.05; data are represented as mean ± SEM).
 (E) Estimation of intratumoral heterogeneity in breast-BrMs (see STAR Methods for details; kataeic, n = 4; non-kataeic, n = 5 biological replicates; two-tailed unpaired Mann-Whitney test *p < 0.05). See also Tables S1–S5.



(legend on next page)

in breast metastatic cancers, including *ESR1* mutation (Figure 2A; Table S2) and *ARID1A* loss (Figures S3C and S3D; Tables S4 and S5⁴⁴). Similar to our findings in lung-BrMs, the average TMB of our breast-BrM cohort was higher than that of primary breast tumors in TCGA (Figure 2B). Notably, four breast-BrMs (BrM35, BrM65, BrM167, and BrM169) presented the highest mutational load and showed a distinct mutational pattern, dominated by transitions and transversions at C:G pairs (Figure 2A). Mutational signature analyses further indicated that signatures 2 and 13 account for a large proportion of the mutations observed in these BrMs (Figure 2A). Both of these signatures have been attributed to the activity of the APOBEC/AID family of deaminases and frequently appear together.⁴² APOBECs have been implicated in the generation of hypermutation clusters in small genomic regions, also known as kataegis, which have been observed in multiple primary tumors, including breast cancer.^{42,45,46} We indeed detected kataegis in the four above-mentioned breast-BrMs: BrM35, BrM65, BrM167, and BrM169 (Figure 2C). Three out of four of these samples are HER2⁺ (Figure 2A), in line with previous findings reporting an association between kataegis and elevated HER2 levels in primary breast tumors.⁴⁷ As expected, we detected a higher number of mutations (Figure 2D) and greater ITH (Figures 2E, S5B, and S5C) in kataegic vs. non-kataegic BrMs.

Importantly, the findings presented above were recapitulated in our independently collected validation cohort (Figure S6 and Table S3). The prevalence of *TP53*^{mut}, *TP53*^{mut};*KRAS*^{mut}, and NP/NK tumors in the lung-BrM validation cohort paralleled that of the lung-BrM immunogenomics cohort (*TP53*^{mut} > *TP53*^{mut};*KRAS*^{mut}). There was also concordance when comparing the proportions of kataegic breast-BrMs between the immunogenomics and validation cohorts (44% vs. 31% kataegic tumors, respectively; Figure S6 and Table S3). We found similar results in terms of average TMB vs. primary tumors, with both lung- and breast-BrMs showing a similar but slightly higher mutational burden compared with their primary counterparts (Figures S6B and S6F). Moreover, differences in mutational load and ITH between genetically distinct lung- and breast-BrMs were conserved in the validation cohort (Figures S6C, S6D, and S6G). Lastly, mutational signatures associated with oncogenic events presumably originating from primary tumors were also identified (Figures S6A and S6E), reinforcing the notion that lung- and breast-BrMs retain the mutational footprint of their tumors of origin.

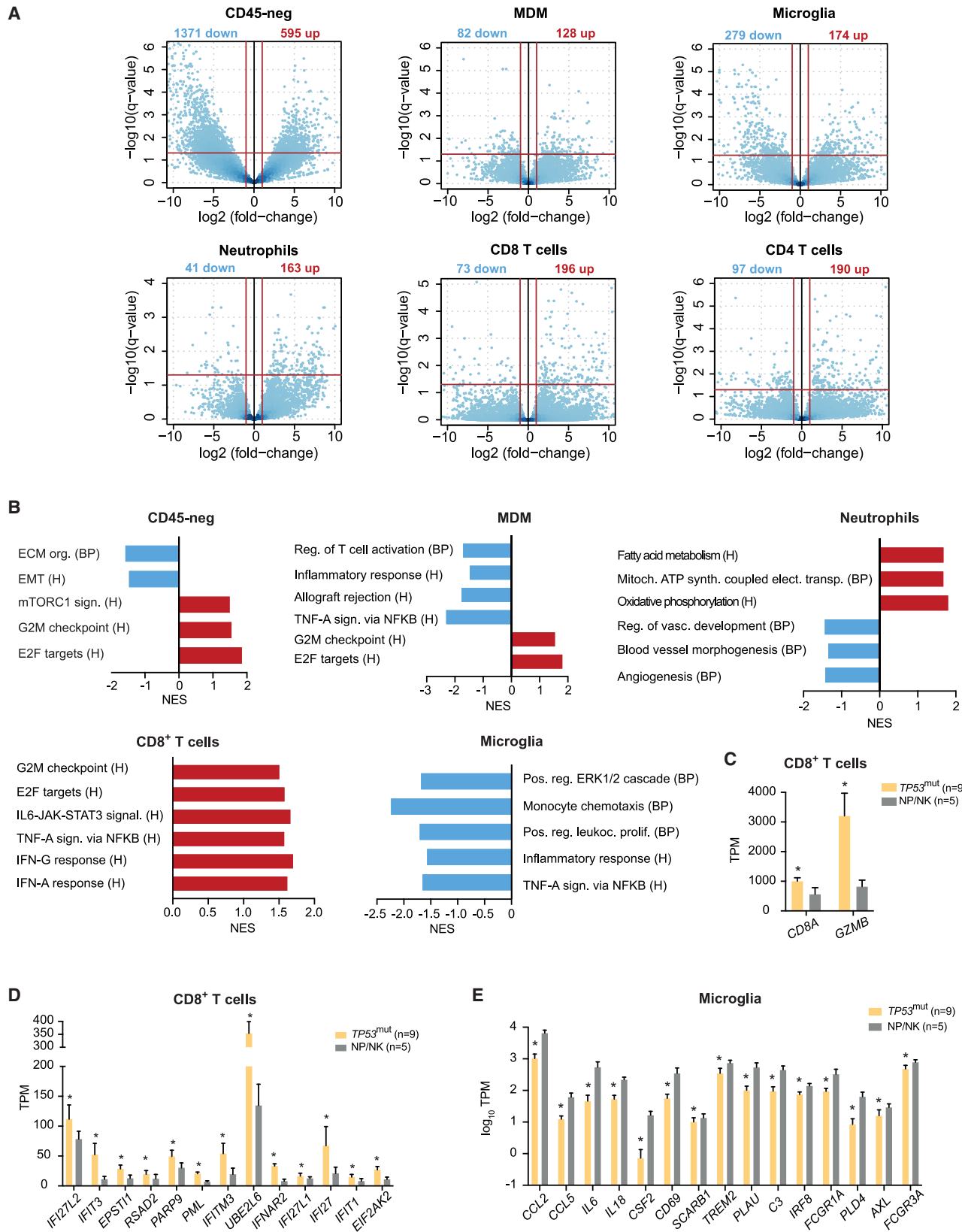
Characteristic immune cell landscapes in genetically distinct lung-BrMs

To next explore the TIME composition in these genetically distinct lung-BrMs, we performed multiparameter FCM analysis and quantified overall immune infiltrates and the relative abundance of 14 different immune cell populations. This revealed a significant increase in immune cell infiltration in *TP53*^{mut} lung-BrMs when compared with their NP/NK counterparts, as reflected by a larger proportion of lymphoid (CD45⁺ CD11B⁻) and myeloid (CD45⁺ CD11B⁺) cells than of non-immune (CD45-negative) cells (Figure 3A). Interestingly, this aligns well with previously published data showing that *TP53* mutations correlate with a higher leukocyte infiltration in many primary cancers.¹⁹ Within the immune compartment, we observed a significant decrease in the proportion of microglia (Kruskal-Wallis *p* = 0.01; Dunn's multiple comparisons test, adjusted *p* = 0.0016), and a concomitant trend toward an increase in the proportion of CD8⁺ T cells, CD4⁺ T cells, B cells, and neutrophils of total CD45⁺ leukocytes in *TP53*^{mut} vs. NP/NK BrMs (Figure 3B; Kruskal-Wallis and Dunn's multiple comparisons test, adjusted *p* > 0.05).

We next assessed whether phenotypic alterations are also observed between BrMs with different genetic profiles by performing RNA-seq of the major cell populations, including sorted CD45-negative cells (CD45-neg), monocyte-derived macrophages (MDM), microglia, neutrophils, CD8⁺ T cells, and CD4⁺ T cells. We performed differential expression analyses comparing all available sorted populations from *TP53*^{mut} (*n* = 8–9 samples per cell population), *TP53*^{mut};*KRAS*^{mut} (*n* = 4–5 per population), and *KRAS*^{mut} (*n* = 2 per population) lung-BrMs individually against NP/NK lung-BrMs (*n* = 3–5 per population) (Figure 3C; Table S1A; Table S8). These analyses showed widespread transcriptional differences in immune cells, which were generally more evident in *TP53*^{mut} than in *KRAS*^{mut} lung-BrMs (Figure 3C; Table S8). To further investigate whether mutations in *TP53* or *KRAS* alone would have a more pronounced effect on the TIME, we intersected significantly up- and downregulated genes from all contrasts in all sorted immune populations (Figure 3D). These comparisons showed that *TP53*^{mut};*KRAS*^{mut} lung-BrMs are more similar to *TP53*^{mut} than to *KRAS*^{mut} BrMs, suggesting that *TP53* disruption plays a more prominent role in shaping the transcriptional programs of the TIME compared

Figure 3. Characteristic immune landscapes in genetically distinct lung-BrMs

- (A) Flow cytometry (FCM) quantification of non-immune cells (CD45-neg), lymphocytes (CD45⁺, CD11B⁻), and myeloid cells (CD45⁺, CD11B⁺) in lung-BrMs (NP/NK *n* = 5; *KRAS*^{mut} *n* = 2; *TP53*^{mut} *n* = 9; *TP53*^{mut};*KRAS*^{mut} *n* = 5 biological replicates; Kruskal-Wallis plus Dunn's multiple comparisons test *adjusted *p* < 0.05).
- (B) Mean of 14 different immune cell populations analyzed in lung-BrMs as percentage of total CD45⁺ cells. NK, natural killer; DN, double-negative; Treg, regulatory T cells; mono, monocytes; MDM, monocyte-derived macrophages; DC, dendritic cells; iMC, immature myeloid cells; see STAR Methods for details on the markers used to define individual populations.
- (C) Summary of differential gene expression analyses by DESeq2 (contrasts: *TP53*^{mut} vs. NP/NK; *KRAS*^{mut} vs. NP/NK; *TP53*^{mut};*KRAS*^{mut} vs. NP/NK). Only genes with an adjusted *p* value ≤ 0.05 and absolute fold-change ≥ 2 were defined as differentially expressed. Black, total number of differentially expressed genes (DEGs); red, number of upregulated genes; blue, number of downregulated genes.
- (D) Visualization of intersects of DEGs between genetically distinct BrMs in sorted immune (MDM, microglia, neutrophils, CD8⁺ T cells, CD4⁺ T cells) and non-immune (CD45-neg) populations. Left panel indicates total number of DEGs (up, upregulated genes; down, downregulated genes); number of intersecting genes for each comparison, as encoded in the combination matrix, are indicated above individual bars; numbers below the combination matrix show percentage of intersecting genes for each comparison.
- (E) Circos representation of selected significantly enriched pathways in sorted immune and non-immune populations (gene set enrichment analysis (GSEA) on MSigDB HALLMARK (H) and Gene Ontology Biological Process (BP) gene sets; adjusted *p* ≤ 0.05). Outer rings show genotype of the BrM samples (left half), and whether enrichment scores are positive (red, indicates enrichment in upregulated genes) or negative (blue, indicates enrichment in downregulated genes) (right half). See also Tables S6A and S7A.



(legend on next page)

with *KRAS* gain of function. It is important to note that mutations in *TP53* and *KRAS* presented similar variant allele frequencies in *TP53*^{mut};*KRAS*^{mut} BrMs, indicating that both mutations occurred at a similar time point during tumor evolution, thereby excluding the possibility that an earlier acquisition of *TP53* mutations was responsible for the observed higher similarity between *TP53*^{mut} and *TP53*^{mut};*KRAS*^{mut} lung-BrMs (Table S2).

We functionally annotated alterations in gene expression by gene set enrichment analysis (GSEA⁴⁸) on MSigDB,⁴⁹ HALLMARK (H), and Gene Ontology Biological Process (BP) gene sets, establishing a significance threshold of adjusted p value ≤ 0.05 (Figure 3E; Table S8; Table S10A). CD45-neg cells from *TP53*^{mut} and *TP53*^{mut};*KRAS*^{mut} tumors displayed a more proliferative transcriptional signature than NP/NK tumors, as evidenced by a positive enrichment of proliferation-related pathways, such as “E2F targets,” “MYC targets,” and “G2M checkpoint” (Figure 3E). While the CD45-neg fraction may also contain other non-immune cells, including neurons and astrocytes, it is reasonable to conclude that given the low proliferation rate of these cells in the brain, these observed transcriptional differences are mostly driven by the cancer cells. Overrepresentation analysis (ORA) on differentially expressed genes (DEGs) validated these results (upregulated genes were enriched in “cell division,” “cell cycle,” “nuclear division” pathways (BP); adjusted $p < 0.05$) and further revealed a significant enrichment of down-regulated genes in the “endocytosis” pathway in *TP53*^{mut} vs. NP/NK tumors (KEGG v7.4, adjusted $p < 0.05$) (Table S10A). Interestingly, dysregulated endocytosis has been reported to contribute to several hallmarks of cancer, including reduced apoptosis, sustained proliferation, and enhanced invasiveness.^{50,51} This may provide an explanation for the high prevalence of *TP53* mutations in lung-BrMs (this study and Schaeffler et al., Robinson et al., and Shih et al.^{13,31,32}).

A wide range of transcriptional alterations was also observed in the immune compartment of *TP53*^{mut}, *KRAS*^{mut}, and *TP53*^{mut};*KRAS*^{mut} lung-BrMs when compared with NP/NK tumors (Figure 3E; Table S8; Table S10A). MDMs and microglia showed a generally more immunosuppressive phenotype, characterized by negative enrichment of pro-inflammatory pathways, including “inflammatory response,” “positive regulation of immune response,” “positive regulation of T cell activation” and “IFN- γ response” (Figure 3E). These changes were shared by *TP53*^{mut}, *KRAS*^{mut}, and *TP53*^{mut};*KRAS*^{mut} lung-BrMs. Conversely, transcriptional alterations in CD8⁺ T cells were only detected in *TP53*^{mut} and *TP53*^{mut};*KRAS*^{mut} lung-BrMs and were linked to a more activated-like phenotype, as shown by a positive enrichment in proliferation-related (“E2F targets,” “G2M checkpoint”) and activation-related (“IFN- γ response,” “IFN- α response,” “TNF- α signaling via NF- κ B,” “IL6-JAK-STAT3 signaling”) pathways (Figure 3E).

The greatest differences in gene expression of the CD4⁺ T cell population were observed in *KRAS*^{mut} lung-BrMs, which showed a more immunosuppressive and less pro-angiogenic transcriptional status, defined by negative enrichment in pro-inflammatory (“TNF- α signaling via NF- κ B,” “inflammatory response,” “positive regulation of lymphocyte activation”) and pro-angiogenic (“vasculature development,” “angiogenesis”) pathways (Figure 3E).

In sum, these results reveal that genetically distinct lung-BrMs present characteristic immunophenotypes, with *TP53*^{mut} lung-BrMs being associated with the largest alterations in the composition and transcriptional landscape of the TIME.

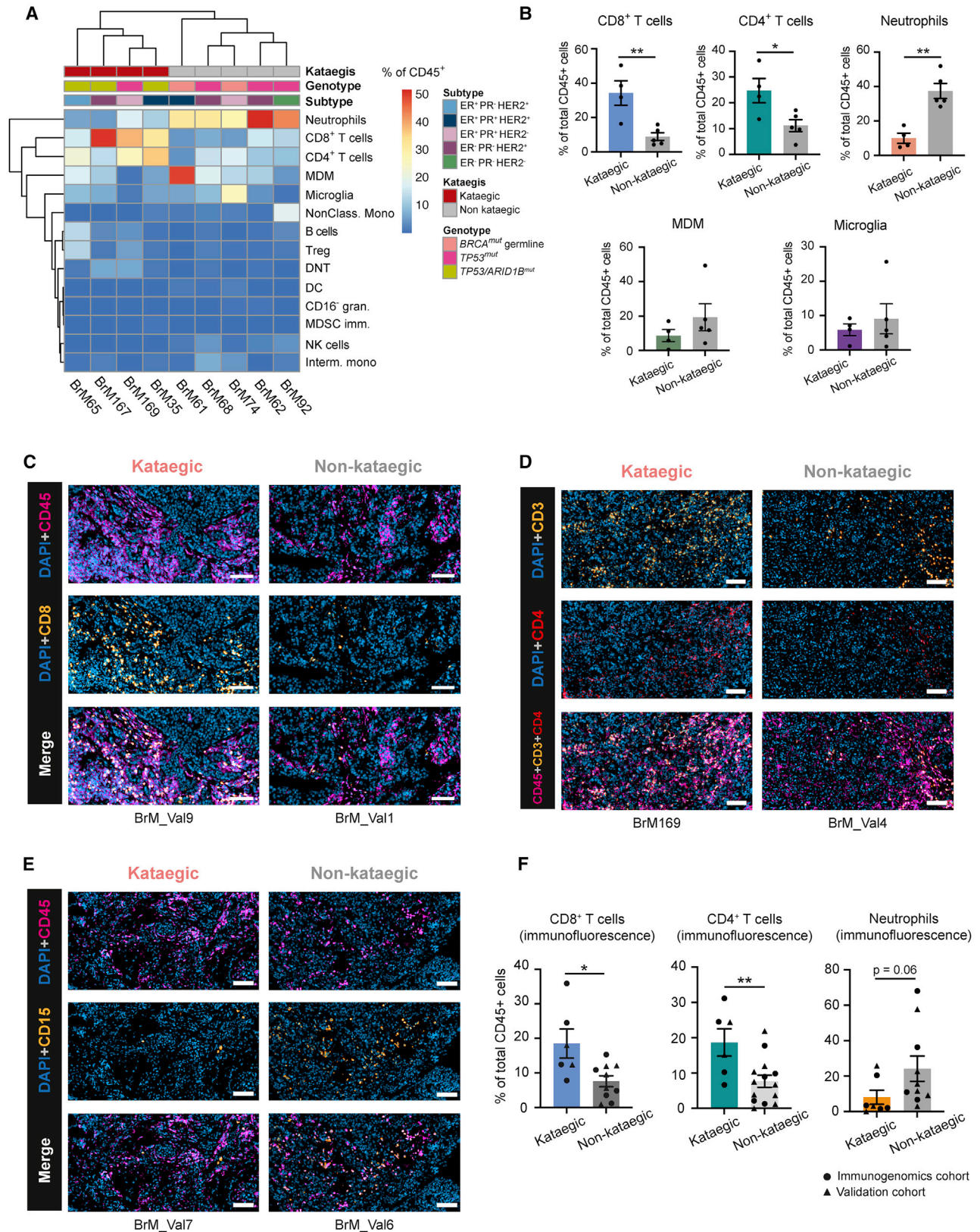
TP53 mutant lung-BrMs present a distinctive immune landscape

We next focused on further dissecting the widespread transcriptional alterations observed in the TIME of *TP53*^{mut} lung-BrMs (Figure 4A). GSEA revealed higher type I and type II interferon responses and increased IL6-JAK-STAT3 and NF- κ B signaling in CD8⁺ T cells (Figures 4B, S7A; Table S10A), indicating that CD8⁺ T cells from *TP53*^{mut} lung-BrMs are more activated than those from NP/NK tumors. In line with these findings, we observed a significant upregulation of genes related to T cell activation, such as *GZMB* (Figure 4C), and interferon responses, including *IFNAR2*, *IFI27L2*, *IFIT1*, *IFIT3*, *IFITM3*, *IFI27*, and *IFI27L1* (Figure 4D). In addition, gene set variation analyses (GSVA) showed significantly higher scores for “TCR signaling” and “Cytotoxic T lymphocyte (CTL)” reactivity pathways (Figure S7B) in CD8⁺ T cells isolated from *TP53*^{mut} compared with NP/NK lung-BrMs, indicating a more activated status for these cells. To further interrogate the functional state of CD8⁺ T cells, we queried the expression of exhaustion-related markers. We found a trend toward higher mRNA levels of the co-inhibitory receptors *HAVCR2*, *LAG3*, *PD-1*, *TIGIT*, and *CTLA-4* (Figure S7C; DESeq2 analysis, adjusted $p > 0.05$) in *TP53*^{mut} vs. NP/NK lung-BrMs and also of the transcription factor *BATF*, which has been reported to drive CD8⁺ T cells from exhaustion into a more responsive state.^{52,53} Whether this indicates ongoing T cell exhaustion or rather reflects CD8⁺ T cells pivoting away from this condition toward a more effector-like state is an interesting point for future investigation.

Within the myeloid cell compartment, neutrophils from *TP53*^{mut} lung-BrMs showed transcriptional evidence of increased mitochondrial activity, oxidative phosphorylation, fatty acid metabolism, and DNA repair and reduced expression of genes involved in vascular development and angiogenesis (Figures 3E and 4B). This may be suggestive of a metabolic switch toward mitochondrial fatty acid oxidation to support ROS production and exert an immunosuppressive function under limited glucose supply in the tumor microenvironment, as

Figure 4. Transcriptional analysis of the immune microenvironment of TP53 mutant lung-BrMs

- (A) Volcano plot representation of DEG in *TP53*^{mut} vs. NP/NK lung-BrMs in sorted immune and non-immune cell populations. Horizontal and vertical red lines indicate adjusted p value (≤ 0.05) and fold-change thresholds (≥ 2) respectively for genes to be considered differentially expressed.
 (B) Normalized enrichment score (NES) of selected gene sets from the MSigDB hallmark (H) and Gene Ontology BP collections in sorted CD45-neg cells, MDMs, neutrophils, CD8⁺ T cells, and microglia (adjusted p value ≤ 0.05).
 (C and D) Normalized counts (TPM, transcripts per million) of T cell activation-related genes (C) and interferon response-related genes (D) in sorted CD8⁺ T cells.
 (E) Normalized counts of selected genes in sorted microglia; please note log₁₀ scale (C–E, *TP53*^{mut} n = 9; NP/NK n = 5 biological replicates; adjusted p values from differential expression analysis by DESeq2; *adjusted $p < 0.05$; data are represented as mean \pm SEM). See also Tables S6A and S7A.



(legend on next page)

previously reported in a mouse model of primary breast cancer.⁵⁴ MDMs and microglia displayed a less activated, less phagocytic, and more immunosuppressive transcriptional program. This was evidenced by overall negative GSEA enrichment scores in pathways related to MDM/microglia activation (“TNF- α signaling via NF- κ B,” “positive regulation of ERK1/2 cascade”) and inflammation (“inflammatory response,” “allograft rejection,” “regulation of T cell activation,” “lymphocyte migration,” “lymphocyte activation,” etc.) (Figures 4C, S7D, and S7E; see Table S10A for a full list of pathways and core enrichment genes). Furthermore, we observed a significant downregulation of pro-inflammatory cytokines, such as *CCL2*, *CCL3*, *CCL4*, *CCL5*, *IL6*, *IL7*, and *IL18*; activation-related genes, including *CD69* and *TREM2*; a well-known mediator of neuroinflammation, *CSF2*; and genes related to phagocytosis, such as *AXL*, *SCARB1*, *FCGR1A*, and *FCGR3A* (Figures 4E and S7F). Finally, *IL1R1* and *IL1R2* were significantly upregulated in microglia (and showed a trend toward higher expression in MDMs) of *TP53*^{mut} vs. NP/NK lung-BrMs (Table S8). *IL1R* has been implicated in fostering immunosuppression by tumor-associated macrophages in a melanoma model,⁵⁵ suggesting that *IL1R* signaling could contribute to the immunosuppressive phenotype observed in microglia.

Overall, our data reveal that *TP53*^{mut} lung-BrMs present a distinctive TIME, characterized by a higher immune infiltration, increased CD8⁺ T cell activation, and a more immunosuppressive myeloid cell compartment.

Kataegic breast-BrMs display a more inflamed tumor microenvironment

Genomic characterization of breast-BrMs identified a subset of tumors in which kataegis, i.e., focalized hypermutation, was detected (Figure 2). These tumors presented with a higher mutational burden, neoantigen load, and increased intratumoral heterogeneity (Figures 2D, 2E, S5B, and S5C). To determine whether this mutational phenotype was associated with a distinct TIME, we performed multicolor FCM and RNA-seq of purified immune and non-immune populations. Unsupervised clustering of breast-BrM samples based on the relative abundance of 14 different immune populations indicated that the composition of the TIME of kataegic breast-BrMs was indeed unique and defined by a higher CD8⁺ and CD4⁺ T cell abundance and lower neutrophil infiltration (Figures 5A and 5B). These results were further validated by immunofluorescence staining (Figures 5C–5F).

Differential expression analysis contrasting sorted populations from kataegic and non-kataegic breast-BrMs revealed extensive transcriptional alterations in non-immune (CD45-neg, 527 DEG) and immune cells (CD8⁺ T cells, 94 DEGs; CD4⁺ T cells, 384

DEGs; MDM, 46 DEGs; microglia, 37 DEGs; neutrophils, 322 DEGs; absolute fold-change ≥ 2 and adjusted p value ≤ 0.05 ; Table S9). GSEA showed that CD45-neg cells display a more pro-inflammatory phenotype, supported by a positive enrichment of inflammation-related pathways such as “Positive regulation of *IL1B* production,” “Positive regulation of defense response,” “Allograft rejection,” and “Inflammatory response” (Figure 6A, Table S10B). Likewise, the myeloid cell compartment also showed a generally more inflamed status, as demonstrated by the positive GSEA enrichment in interferon alpha response pathway found in MDMs, microglia, and neutrophils (Figure 6A; Table S10B). In line with these findings, neutrophils from kataegic tumors showed a significant upregulation of several genes coding for pro-inflammatory S100 proteins (*S100A2*, *S100A7*), pro-inflammatory cytokines (*IL18*, *IL1F10*), IFN response genes (*IFI27*, *IFI44L*, *VAMP8*), and degranulation-related genes (*SLPI*, *GSTP1*, *GGH*) (Figure 6B; Table S9). Interestingly, this may be connected with the more activated phenotype displayed by MDMs from kataegic breast-BrMs, since S100 proteins have been implicated in macrophage inflammation.⁵⁶ It is also intriguing that neutrophils from kataegic breast-BrMs showed a trend toward upregulation of *CXCL10* (adjusted p = 0.06; DESeq2 analysis), a pro-inflammatory cytokine involved in the recruitment of effector T cells,⁵⁷ which could account for the higher CD8⁺ T cell infiltration observed in kataegic breast-BrMs (Figures 6B and 5; Table S9). CD8⁺ T cells from kataegic tumors also presented a more activation-like phenotype. This was evidenced by an increased type I interferon response (Figure 6C; Table S10B) and GSVA showing significantly higher scores in several T cell activation-related pathways (“Early CD8 activation,” “AKT phosphorylates targets in the cytosol,” “NFKB is activated and signals survival,” “IKK complex recruitment mediated by RIP1,” “Activation of IRF3/IRF7 mediated by TBK1/IKK ϵ ”) and a lower “apoptotic execution phase” pathway score when comparing kataegic and non-kataegic breast-BrMs (Figure 6D). Accordingly, kataegic breast-BrM tumors exhibited a significantly higher proportion of CD103⁺CD8⁺ T cells (Figures 6E and 6F), which have been previously described to drive cytotoxic effector responses against several tumor types^{58,59} and to correlate with a better response to anti-PD-L1 immunotherapy in lung and bladder primary cancers.⁶⁰ Deconvolution analysis of bulk RNA-seq data further validated these results, confirming a higher infiltration of cytotoxic CD8⁺ T cells (1.95 \times fold increase) in kataegic vs. non-kataegic breast-BrMs (Figure 6G).

Together, our results indicate that kataegic breast-BrMs present a characteristic TIME, defined by an increased CD8⁺ and CD4⁺ T cell infiltration, reduced neutrophil presence, and an

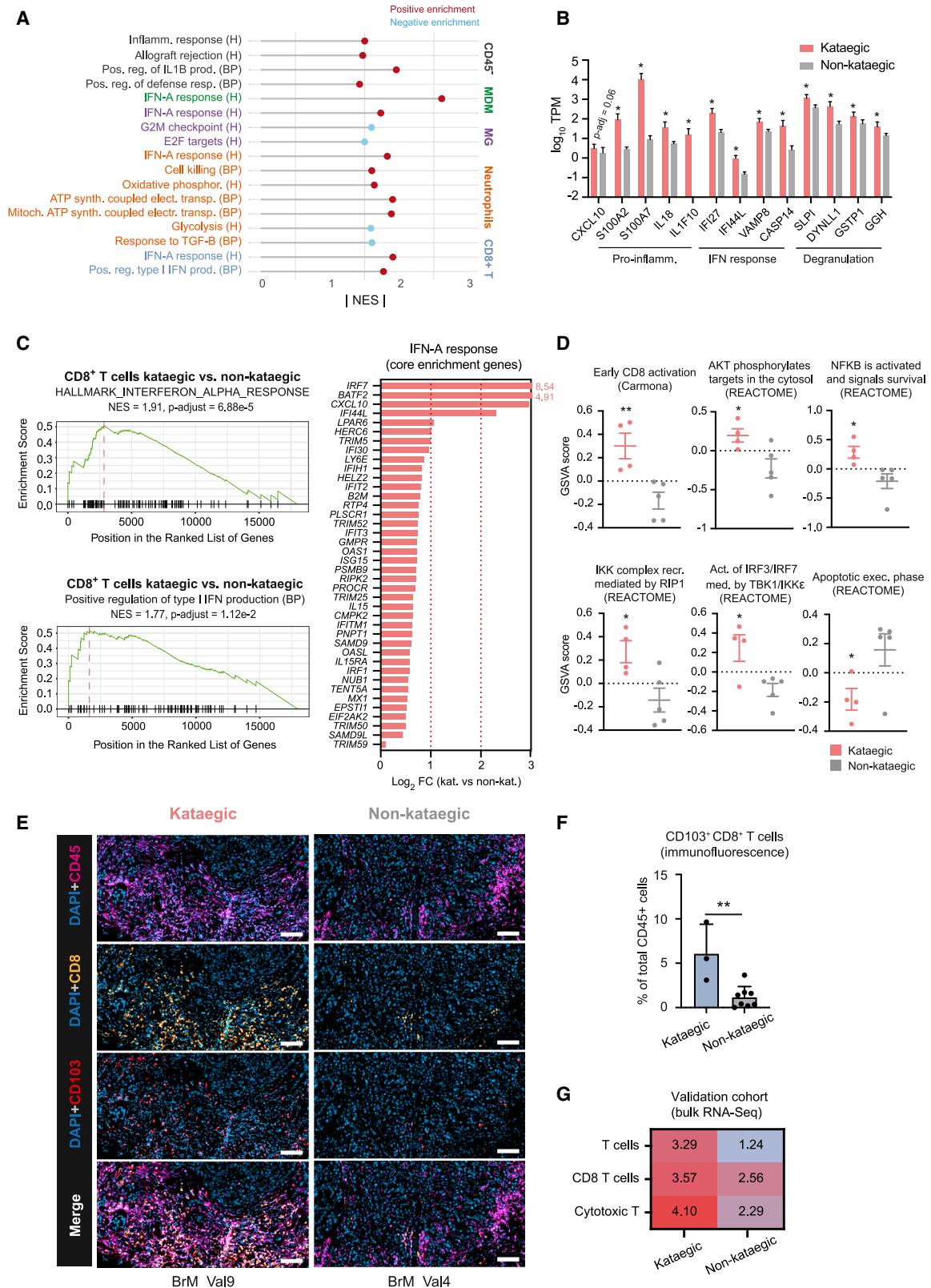
Figure 5. Kataegic breast-BrMs present a distinct immune microenvironment

(A) Unsupervised clustering of different immune cell fractions (of total CD45⁺ immune cells) as quantified by FCM.

(B) FCM quantification of the abundance of selected immune populations in kataegic and non-kataegic breast-BrMs (kataegic, n = 4; non-kataegic, n = 5 biological replicates; unpaired two-tailed t test, *p < 0.05, **p < 0.01; data are represented as mean \pm SEM).

(C–E) Representative immunofluorescence staining of (C) CD8⁺ T cells, (D) CD4⁺ T cells, and (E) CD15⁺ neutrophils in breast-BrM tumors.

(F) Quantification of CD8⁺ T cells, CD4⁺ T cells, and neutrophils from immunofluorescence stainings of kataegic and non-kataegic breast-BrMs from the immunogenomics and validation (Val) cohorts (CD8⁺ T cells: kataegic, n = 6; non-kataegic, n = 10 biological replicates; neutrophils: kataegic, n = 7; non-kataegic, n = 10 biological replicates; unpaired two-tailed Mann-Whitney test, *p < 0.05; data are represented as mean \pm SEM). Only samples with a false to true positive ratio <2% were included in these analyses (see STAR Methods for details). The two samples closest to the mean of each group were selected as representative for the images shown in (C)–(E). Scale bars represent 100 μ m.



(legend on next page)

overall more pro-inflammatory phenotype compared with non-kataegic BrMs.

DISCUSSION

Metastatic brain tumors are associated with a very poor prognosis, with survival rates for patients diagnosed with BrM often measured in months.³ Although new therapeutic strategies are emerging and include personalized treatments based on the genetic makeup of primary tumors, along with immune-based therapies,^{3,5,6,63,64} only a small subset of patients with BrM respond to current treatments.^{4,7,9–11} This is likely related to the phenotypic heterogeneity of the TIME, which can be influenced by genetic alterations, as previously reported for several primary cancers.^{15,18–22,24–26,65} However, the extent to which specific genetic profiles correlate with, and potentially shape, distinct immune states in the TIME of BrMs is unknown. In this study, we therefore integrated next-generation sequencing and antibody-based immunophenotyping analyses to extensively characterize the immunogenomic landscape of lung- and breast-BrMs. By leveraging the combined analyses of DNA sequencing of tumors, RNA sequencing of immune populations, multiparametric flow cytometry, and immunofluorescence analyses of whole tissue samples, we have uncovered specific immunophenotypes associated with distinct genetic alterations in human lung- and breast-BrMs.

Previous studies have reported on the relevance of the TIME in shaping responses to immunotherapy in primary human cancers. For example, immunogenomic analyses of 33 different primary cancer types in TCGA revealed six immune subtypes characterized by distinct somatic alterations, tumor microenvironments, and survival rates.¹⁹ This study also found that mutations in *TP53* correlated with higher overall leukocyte abundance across the cancers analyzed. A recent large-scale transcriptomic characterization of cancer patients identified four microenvironment subtypes that are conserved in multiple primary tumors and correlate with response to immunotherapy.²¹ Interestingly, this study defined an “immune enriched, non-fibrotic” subtype, which is characterized by a high mutational burden, abundant T cell infiltration, and the presence of immune-suppressive cells, as a biomarker associated with a better response to immunotherapy.²¹ Moreover, in NSCLC, a “lung cancer immune activa-

tion module,” characterized by *PDCD1*⁺ *CXCL13*⁺ activated T cells, *SPP1*⁺ macrophages, and *IgG*⁺ plasma cells, was identified by scRNA-seq profiling of early-stage tumors. Importantly, this module was also associated with a higher mutational burden, ectopic antigens, and *TP53* mutations, and it correlated with a better response to anti-PD(L)-1 immunotherapy.²²

Together, these phenotypes are remarkably similar to what we have uncovered herein in *TP53*^{mut} lung-BrMs, which are characterized by a high mutational burden, increased T cell infiltration, and the presence of a more immunosuppressive myeloid compartment. This suggests that immune checkpoint blockade (ICB) might be a particularly beneficial treatment for patients with *TP53*^{mut} lung-BrMs. Moreover, we detected a significant upregulation of *IL1R1* and *IL1R2* in microglia and a significant downregulation of *TREM2* in microglia and MDMs from *TP53*^{mut} lung-BrMs when compared with NP/NK BrMs. It has been reported that *IL1R* fosters immune suppression by tumor-associated macrophages in melanoma, and consequently that combinatorial immunotherapy targeting *IL1R* signaling and PD-1 resulted in anti-tumoral effects in the pre-clinical setting.⁵⁵ *TREM2* inhibition was also shown to lead to enhanced T cell activity and improved response to anti-PD1 immunotherapy in several mouse models.⁶⁶ Together, these mechanistic findings support our prediction that *TP53*^{mut} lung-BrMs specifically would show a better response to immunotherapy. Finally, a high non-synonymous mutational burden—often a proxy for the increased presence of immunogenic neoantigens—has been linked to an improved response to ICB in NSCLC.^{67,68} We identified both a greater mutational burden and a higher level of neoantigens as characteristic features of *TP53*^{mut} lung-BrMs when compared with NP/NK BrMs, further reinforcing the notion that these *TP53*^{mut} BrMs may be more sensitive to immunotherapy.

Immune-modifying effects of TMB and mutational status of driver genes directly impacting the response to immunotherapy have also been recently reported in breast cancer. In primary breast tumors, *BRCA1* and *BRCA2* mutations lead to distinct TIME phenotypes, with *BRCA2* truncating mutations resulting in a more immunogenic TIME and an improved ICB response.⁶⁵ Likewise, homologous recombination deficiency, linked to higher mutational burden and genomic instability, has been recently identified as a key vulnerability in breast-BrM patients treated with PARP inhibitors.⁶⁹ Kataegis, or focalized hypermutation,

Figure 6. Transcriptional analysis of the immune microenvironment of kataegic and non-kataegic breast-BrM tumors

- (A) NES of selected gene sets from the MSigDB hallmark (H) and Gene Ontology BP collections in sorted CD45-neg cells, MDMs, microglia, neutrophils, and CD8⁺ T cells (adjusted p value ≤ 0.05).
- (B) Normalized counts (TPM) of selected genes in sorted neutrophils (kataegic, n = 4; non-kataegic, n = 5 biological replicates; adjusted p values from differential expression analysis by DESeq2; *adjusted p < 0.05; data are represented as mean \pm SEM).
- (C) GSEA of interferon alpha response genes (MSigDB H collection; upper left panel) and genes involved in positive regulation of type I interferon production (Gene Ontology Biological Process collection; lower left panel) in sorted CD8⁺ T cells; top 40 interferon alpha response genes sorted by fold change (kataegic vs. non-kataegic; numbers in pink indicate log₂ fold changes) from DESeq2 analysis (right panel).
- (D) Gene set variation analysis (GSVA) of “Early CD8 activation” (as defined in Andreatta et al.⁶¹), AKT, NFKB, and apoptosis pathway-related gene sets from the Reactome database in sorted CD8⁺ T cells. Each dot corresponds to one BrM sample (kataegic, n = 4; non-kataegic, n = 5 biological replicates; unpaired two-tailed t test, *p < 0.05; **p < 0.01; data are represented as mean \pm SEM).
- (E and F) (E) Representative immunofluorescence staining and (F) quantification of CD103⁺CD8⁺ T cells in breast-BrM tumors from the validation cohort (kataegic, n = 3; non-kataegic, n = 8 biological replicates; unpaired two-tailed t test, **p < 0.01; data are represented as mean \pm SD). Only samples with a false to true positive ratio <2% were included in these analyses (see STAR Methods for details). Scale bars represent 100 μ m.
- (G) Heatmap of the average immune cell Danaher scores (computed as in Danaher et al.⁶²) from bulk RNA-seq of breast-BrM samples from the validation cohort (n = 13). See also Tables S6B and S7B.

occurs in approximately 55% of breast cancers and is associated with increased genomic instability, HER2 positivity, and transcriptome-wide expression changes, resulting in lower invasive potential and better patient prognosis.⁴⁷ Accordingly, our immunogenomic analysis of breast-BrMs revealed that hypermutated tumors (75% of which are also HER2⁺) present a more inflamed TIME overall, characterized by increased T cell infiltration and broad transcriptional changes in cancer cells (CD45-neg) and immune cells leading to a pro-inflammatory phenotype. Furthermore, we found that neutrophils from kataegic BrMs express higher levels of CXCL10, a cytokine involved in the recruitment of effector T cells, which has recently been shown to predict better responses of anti-PD1 treatment in metastatic melanoma,⁷⁰ and that kataegic BrMs present a significantly higher proportion of CD103⁺CD8⁺ T cells, a predictor of improved responses to PD1 blockade in some primary cancers.⁶⁰ Together, these findings suggest that patients with kataegic breast-BrMs might benefit from ICB and/or PARP inhibition therapies.

While we cannot currently evaluate how these individual alterations differentially sculpt the TIME in a dynamic manner, due to the lack of appropriate genetic mouse models, this study nonetheless provides compelling evidence for an association between specific genetic alterations and unique TIME immunophenotypes in human BrMs. This knowledge can be of critical importance to predict responses to current immunotherapies, to stratify patients, and to develop novel immune-based personalized treatments guided by the genetic makeup of the tumors. In this regard, genotyping of biopsied or surgically resected primary tumors or genetic profiling of circulating tumor cells or circulating free DNA from cerebrospinal fluid⁷¹ could represent valid surrogate approaches to inform customized immune therapies for BrM patients. Different breast and lung-BrM mouse models are under active development, and further research will be critical to dissect the precise contribution of specific genetic alterations to the composition and status of the immune micro-environment of BrMs. We expect that our results herein will inform these fundamental next steps to advance toward the goal of personalized and more effective therapies for BrM patients.

Limitations of the study

There are some limitations to our study. Firstly, it does not include matched primary tumor samples, so we cannot ascertain whether the phenotypes described here are metastasis specific, although in some cases (*TP53*^{mut} lung-BrMs), they are similar to published data on primary tumors. Secondly, the number of *TP53*^{WT}/*KRAS*^{mut} lung-BrMs analyzed in this study is limited, which may preclude the identification of relevant TIME phenotypes. While this study could benefit from a larger sample size, we nonetheless demonstrate that our findings are not driven by potentially confounding factors, such as primary tumor subtype, treatment, age, or sex. Due to the current lack of appropriate genetic mouse models, we could not test whether the observed genetic makeups are causative of the TIME phenotypes reported. Different pre-clinical breast and lung-BrM models are under active development and will be important to assess this question and to evaluate whether BrMs with distinct genetic makeups and TIMEs respond differently to immunotherapy.

STAR★METHODS

Detailed methods are provided in the online version of this paper and include the following:

- KEY RESOURCES TABLE
- RESOURCE AVAILABILITY
 - Lead contact
 - Materials availability
 - Data and code availability
- EXPERIMENTAL MODEL AND SUBJECT DETAILS
- METHOD DETAILS
 - Clinical sample processing, flow cytometry, fluorescence-activated cell sorting, immunofluorescence, DNA sequencing and RNA sequencing of sorted populations
 - Flow cytometry markers and definition of cell populations for fluorescence-activated cell sorting
 - RNA-sequencing of sorted immune cell populations
 - Bulk RNA-sequencing of validation cohort samples
 - Whole-exome and low-pass whole-genome sequencing
 - Immunofluorescence (IF) staining and quantification
 - Computational analyses
- QUANTIFICATION AND STATISTICAL ANALYSIS

SUPPLEMENTAL INFORMATION

Supplemental information can be found online at <https://doi.org/10.1016/j.xcrm.2022.100900>.

ACKNOWLEDGMENTS

We would like to express our deepest gratitude to all patients who kindly donated tissue for this study. We thank the neurosurgery/neurooncology clinical team of the Centre Hospitalier Universitaire Vaudois (CHUV), particularly the operating room staff and the technicians at the pathology department, for their support in coordinating patient tissue collection. We are very grateful to members of the Joyce lab for valuable scientific discussions, Drs. Benoit Duc and Sabine Galland for their assistance in annotating clinical information, Drs. Leire Bejarano and Vladimir Wischniewski for their technical assistance during clinical sample processing, members of the Hegi lab for their help in accessing banked human samples, Prof. David Gfeller for excellent advice and insightful discussions on neoantigen predictions, and the Mouse Pathology and Flow Cytometry Core Facilities of UNIL for their valuable technical support. This research was supported in part by the Carigest Foundation, Fondation IS-REC, Ludwig Institute for Cancer Research, and the University of Lausanne (to J.A.J.). A.A.-P. was supported by an EMBO Long-term Postdoctoral Fellowship (EMBO ALTF 654–2019) and is currently supported in part by a Marie Skłodowska Curie Actions Individual Fellowship (MSCA-IF 890933). K.S. was supported in part by an Erwin-Schrödinger Fellowship from the Austrian Science Fund (FWF, J4343-B28). F.K. was supported in part by the German Research Foundation (DFG, KL2491/1–1) and Fondation Medic. Some of the results shown in Figures 1C, 2B, S1A, S6B, and S6F are based on data generated by the TCGA Research Network (<https://www.cancer.gov/tcga>).

AUTHOR CONTRIBUTIONS

A.A.-P. and J.A.J. designed the study. A.A.-P., R.R.M., K.S., F.K., and M.K. processed clinical samples and analyzed flow cytometry data. A.A.-P. performed immunofluorescence stainings and quantifications and all computational analyses. A.A.-P., F.S.K., and V.Z. performed structural predictions for *TP53* mutants. A.F.H., R.T.D., and M.E.H. provided clinical material. S.B.

and J.-P.B. provided histopathological reviews. A.A.-P. prepared the figures. A.A.-P. and J.A.J. wrote the manuscript. J.A.J. supervised the study. All authors reviewed, edited, or commented on the manuscript.

DECLARATION OF INTERESTS

F.K. is currently an employee at Sophia Genetics; V.Z. is a consultant for Cellectia Biotech; S.B. has received honoraria from Eli Lilly (Advisory Board) and research funding to the institution from Roche and Basilea (last 3 years); M.E.H. has an advisory role at TME Pharma; J.A.J. has received honoraria for speaking at research symposia organized by Bristol Meyers Squibb and Glenmark Pharmaceuticals (last 3 years) and currently serves on the scientific advisory board of Pionyr Immunotherapeutics.

Received: May 4, 2022

Revised: September 20, 2022

Accepted: December 19, 2022

Published: January 17, 2023

REFERENCES

- Valiente, M., Ahluwalia, M.S., Boire, A., Brastianos, P.K., Goldberg, S.B., Lee, E.Q., Le Rhun, E., Preusser, M., Winkler, F., and Soffietti, R. (2018). The evolving landscape of brain metastasis. *Trends Cancer* 4, 176–196. <https://doi.org/10.1016/j.trecan.2018.01.003>.
- Boire, A., Brastianos, P.K., Garzia, L., and Valiente, M. (2020). Brain metastasis. *Nat. Rev. Cancer* 20, 4–11. <https://doi.org/10.1038/s41568-019-0220-y>.
- Steindl, A., Brunner, T.J., Heimbach, K., Schweighart, K., Moser, G.M., Niziolek, H.M., Moor, E., Kreminger, J., Starzer, A.M., Dieckmann, K., et al. (2022). Changing characteristics, treatment approaches and survival of patients with brain metastasis: data from six thousand and thirty-one individuals over an observation period of 30 years. *Eur. J. Cancer* 162, 170–181. <https://doi.org/10.1016/j.ejca.2021.12.005>.
- Suh, J.H., Kotecha, R., Chao, S.T., Ahluwalia, M.S., Sahgal, A., and Chang, E.L. (2020). Current approaches to the management of brain metastases. *Nat. Rev. Clin. Oncol.* 17, 279–299. <https://doi.org/10.1038/s41571-019-0320-3>.
- Sperduto, P.W., Yang, T.J., Beal, K., Pan, H., Brown, P.D., Bangdiwala, A., Shanley, R., Yeh, N., Gaspar, L.E., Braunstein, S., et al. (2017). Estimating survival in patients with lung cancer and brain metastases: an update of the graded prognostic assessment for lung cancer using molecular markers (Lung-molGPA). *JAMA Oncol.* 3, 827–831. <https://doi.org/10.1001/jamaoncol.2016.3834>.
- Sperduto, P.W., Jiang, W., Brown, P.D., Braunstein, S., Sneed, P., Wattson, D.A., Shih, H.A., Bangdiwala, A., Shanley, R., Lockney, N.A., et al. (2017). Estimating survival in melanoma patients with brain metastases: an update of the graded prognostic assessment for melanoma using molecular markers (Melanoma-molGPA). *Int. J. Radiat. Oncol. Biol. Phys.* 99, 812–816. <https://doi.org/10.1016/j.ijrobp.2017.06.2454>.
- Goldberg, S.B., Gettinger, S.N., Mahajan, A., Chiang, A.C., Herbst, R.S., Sznol, M., Tsiouris, A.J., Cohen, J., Vortmeyer, A., Jilaveanu, L., et al. (2016). Pembrolizumab for patients with melanoma or non-small-cell lung cancer and untreated brain metastases: early analysis of a non-randomised, open-label, phase 2 trial. *Lancet Oncol.* 17, 976–983. [https://doi.org/10.1016/S1470-2045\(16\)30053-5](https://doi.org/10.1016/S1470-2045(16)30053-5).
- Goldberg, S.B., Schalper, K.A., Gettinger, S.N., Mahajan, A., Herbst, R.S., Chiang, A.C., Lilenbaum, R., Wilson, F.H., Omay, S.B., Yu, J.B., et al. (2020). Pembrolizumab for management of patients with NSCLC and brain metastases: long-term results and biomarker analysis from a non-randomised, open-label, phase 2 trial. *Lancet Oncol.* 21, 655–663. [https://doi.org/10.1016/S1470-2045\(20\)30111-X](https://doi.org/10.1016/S1470-2045(20)30111-X).
- Tawbi, H.A., Forsyth, P.A., Algazi, A., Hamid, O., Hodi, F.S., Moschos, S.J., Khushalani, N.I., Lewis, K., Lao, C.D., Postow, M.A., et al. (2018). Combined nivolumab and ipilimumab in melanoma metastatic to the brain. *N. Engl. J. Med.* 379, 722–730. <https://doi.org/10.1056/NEJMoa1805453>.
- Tawbi, H.A.-H., Forsyth, P.A.J., Hodi, F.S., Lao, C.D., Moschos, S.J., Hamid, O., Atkins, M.B., Lewis, K.D., Thomas, R.P., Glaspy, J.A., et al. (2019). Efficacy and safety of the combination of nivolumab (NIVO) plus ipilimumab (IPI) in patients with symptomatic melanoma brain metastases (CheckMate 204). *J. Clin. Oncol.* 37, 9501. https://doi.org/10.1200/JCO.2019.37.15_suppl.9501.
- Long, G.V., Atkinson, V., Menzies, A.M., Lo, S., Guminski, A.D., Brown, M.P., Gonzalez, M.M., Diamante, K., Sandhu, S.K., Scolyer, R.A., et al. (2017). A randomized phase II study of nivolumab or nivolumab combined with ipilimumab in patients (pts) with melanoma brain metastases (mets): the Anti-PD1 Brain Collaboration (ABC). *J. Clin. Oncol.* 35, 9508. https://doi.org/10.1200/JCO.2017.35.15_suppl.9508.
- Quail, D.F., and Joyce, J.A. (2017). The microenvironmental landscape of brain tumors. *Cancer Cell* 31, 326–341. <https://doi.org/10.1016/j.ccell.2017.02.009>.
- Schaettler, M.O., Richters, M.M., Wang, A.Z., Skidmore, Z.L., Fisk, B., Miller, K.E., Vickery, T.L., Kim, A.H., Chicoine, M.R., Osburn, J.W., et al. (2022). Characterization of the genomic and immunologic diversity of malignant brain tumors through multisector analysis. *Cancer Discov.* 12, 154–171. <https://doi.org/10.1158/2159-8290.CD-21-0291>.
- Strickland, M.R., Alvarez-Breckenridge, C., Gainor, J.F., and Brastianos, P.K. (2022). Tumor immune microenvironment of brain metastases: toward unlocking antitumor immunity. *Cancer Discov.* 12, 1199–1216. <https://doi.org/10.1158/2159-8290.CD-21-0976>.
- Klemm, F., Maas, R.R., Bowman, R.L., Kornete, M., Soukup, K., Nassiri, S., Brouland, J.-P., Iacobuzio-Donahue, C.A., Brennan, C., Tabar, V., et al. (2020). Interrogation of the microenvironmental landscape in brain tumors reveals disease-specific alterations of immune cells. *Cell* 181, 1643–1660.e17. <https://doi.org/10.1016/j.cell.2020.05.007>.
- Friebel, E., Kapolou, K., Unger, S., Núñez, N.G., Utz, S., Rushing, E.J., Regli, L., Weller, M., Greter, M., Tugues, S., et al. (2020). Single-cell mapping of human brain cancer reveals tumor-specific instruction of tissue-invading leukocytes. *Cell* 181, 1626–1642.e20. <https://doi.org/10.1016/j.cell.2020.04.055>.
- Gonzalez, H., Mei, W., Robles, I., Hagerling, C., Allen, B.M., Hauge Okholm, T.L., Nanjaraj, A., Verbeek, T., Kalavacherla, S., van Gogh, M., et al. (2022). Cellular architecture of human brain metastases. *Cell* 185, 729–745.e20. <https://doi.org/10.1016/j.cell.2021.12.043>.
- Angelova, M., Mlecnik, B., Vasaturo, A., Bindea, G., Fredriksen, T., Lafontaine, L., Buttard, B., Morgand, E., Bruni, D., Jouret-Mourin, A., et al. (2018). Evolution of metastases in space and time under immune selection. *Cell* 175, 751–765.e16. <https://doi.org/10.1016/j.cell.2018.09.018>.
- Thorsson, V., Gibbs, D.L., Brown, S.D., Wolf, D., Bortone, D.S., Ou Yang, T.-H., Porta-Pardo, E., Gao, G.F., Plaisier, C.L., Eddy, J.A., et al. (2018). The immune landscape of cancer. *Immunity* 48, 812–830.e14. <https://doi.org/10.1016/j.immuni.2018.03.023>.
- De Mattos-Arruda, L., Sammut, S.-J., Ross, E.M., Bashford-Rogers, R., Greenstein, E., Markus, H., Morganello, S., Teng, Y., Maruvka, Y., Pereira, B., et al. (2019). The genomic and immune landscapes of lethal metastatic breast cancer. *Cell Rep.* 27, 2690–2708.e10. <https://doi.org/10.1016/j.celrep.2019.04.098>.
- Bagaev, A., Kotlov, N., Nomie, K., Svekolkin, V., Gafurov, A., Isaeva, O., Osokin, N., Kozlov, I., Frenkel, F., Gancharova, O., et al. (2021). Conserved pan-cancer microenvironment subtypes predict response to immunotherapy. *Cancer Cell* 39, 845–865.e7. <https://doi.org/10.1016/j.ccell.2021.04.014>.
- Leader, A.M., Grout, J.A., Maier, B.B., Nabet, B.Y., Park, M.D., Tabachnikova, A., Chang, C., Walker, L., Lansky, A., Le Berichel, J., et al. (2021). Single-cell analysis of human non-small cell lung cancer lesions refines tumor classification and patient stratification. *Cancer Cell* 39, 1594–1609.e12. <https://doi.org/10.1016/j.ccell.2021.10.009>.

23. Wellenstein, M.D., Coffelt, S.B., Duits, D.E.M., van Miltenburg, M.H., Slagter, M., de Rink, I., Henneman, L., Kas, S.M., Prekovic, S., Hau, C.-S., et al. (2019). Loss of p53 triggers WNT-dependent systemic inflammation to drive breast cancer metastasis. *Nature* 572, 538–542. <https://doi.org/10.1038/s41586-019-1450-6>.
24. Bezzi, M., Seitzer, N., Ishikawa, T., Reschke, M., Chen, M., Wang, G., Mitchell, C., Ng, C., Katon, J., Lunardi, A., et al. (2018). Diverse genetic-driven immune landscapes dictate tumor progression through distinct mechanisms. *Nat. Med.* 24, 165–175. <https://doi.org/10.1038/nm.4463>.
25. Petralia, F., Tignor, N., Reva, B., Koptyra, M., Chowdhury, S., Rykunov, D., Krek, A., Ma, W., Zhu, Y., Ji, J., et al. (2020). Integrated proteogenomic characterization across major histological types of pediatric brain cancer. *Cell* 183, 1962–1985.e31. <https://doi.org/10.1016/j.cell.2020.10.044>.
26. Wang, Q., Hu, B., Hu, X., Kim, H., Squatrito, M., Scarpace, L., deCarvalho, A.C., Lyu, S., Li, P., Li, Y., et al. (2017). Tumor evolution of glioma-intrinsic gene expression subtypes associates with immunological changes in the microenvironment. *Cancer Cell* 32, 42–56.e6. <https://doi.org/10.1016/j.ccell.2017.06.003>.
27. Brastianos, P.K., Carter, S.L., Santagata, S., Cahill, D.P., Taylor-Weiner, A., Jones, R.T., Van Allen, E.M., Lawrence, M.S., Horowitz, P.M., Cibulskis, K., et al. (2015). Genomic characterization of brain metastases reveals branched evolution and potential therapeutic targets. *Cancer Discov.* 5, 1164–1177. <https://doi.org/10.1158/2159-8290.CD-15-0369>.
28. Fukumura, K., Malgulwar, P.B., Fischer, G.M., Hu, X., Mao, X., Song, X., Hernandez, S.D., Zhang, X.H.-F., Zhang, J., Parra, E.R., et al. (2021). Multi-omic molecular profiling reveals potentially targetable abnormalities shared across multiple histologies of brain metastasis. *Acta Neuropathol.* 141, 303–321. <https://doi.org/10.1007/s00401-020-02256-1>.
29. Nguyen, B., Fong, C., Luthra, A., Smith, S.A., DiNatale, R.G., Nandakumar, S., Walch, H., Chatila, W.K., Madupuri, R., Kundra, R., et al. (2022). Genomic characterization of metastatic patterns from prospective clinical sequencing of 25,000 patients. *Cell* 185, 563–575.e11. <https://doi.org/10.1016/j.cell.2022.01.003>.
30. Robinson, D.R., Wu, Y.-M., Lonigro, R.J., Vats, P., Cobain, E., Everett, J., Cao, X., Rabban, E., Kumar-Sinha, C., Raymond, V., et al. (2017). Integrative clinical genomics of metastatic cancer. *Nature* 548, 297–303. <https://doi.org/10.1038/nature23306>.
31. Shih, D.J.H., Nayyar, N., Bihun, I., Dagogo-Jack, I., Gill, C.M., Aquilanti, E., Bertalan, M., Kaplan, A., D'Andrea, M.R., Chukwueke, U., et al. (2020). Genomic characterization of human brain metastases identifies drivers of metastatic lung adenocarcinoma. *Nat. Genet.* 52, 371–377. <https://doi.org/10.1038/s41588-020-0592-7>.
32. Vassella, E., Kashani, E., Zens, P., Kündig, A., Fung, C., Scherz, A., Herrmann, E., Ermis, E., Schmid, R.A., and Berezowska, S. (2021). Mutational profiles of primary pulmonary adenocarcinoma and paired brain metastases disclose the importance of KRAS mutations. *Eur. J. Cancer* 159, 227–236. <https://doi.org/10.1016/j.ejca.2021.10.006>.
33. Maas, R.R., Soukup, K., Klemm, F., Kornete, M., Bowman, R.L., Bedel, R., Marie, D.N., Álvarez-Prado, Á.F., Labes, D., Wilson, A., et al. (2021). An integrated pipeline for comprehensive analysis of immune cells in human brain tumor clinical samples. *Nat. Protoc.* 16, 4692–4721. <https://doi.org/10.1038/s41596-021-00594-2>.
34. Muiños, F., Martínez-Jiménez, F., Pich, O., Gonzalez-Perez, A., and Lopez-Bigas, N. (2021). In silico saturation mutagenesis of cancer genes. *Nature* 596, 428–432. <https://doi.org/10.1038/s41586-021-03771-1>.
35. Hunter, J.C., Manandhar, A., Carrasco, M.A., Gurbani, D., Gondi, S., and Westover, K.D. (2015). Biochemical and structural analysis of common cancer-associated KRAS mutations. *Mol. Cancer Res.* 13, 1325–1335. <https://doi.org/10.1158/1541-7786.MCR-15-0203>.
36. Cook, J.H., Melloni, G.E.M., Gulhan, D.C., Park, P.J., and Haigis, K.M. (2021). The origins and genetic interactions of KRAS mutations are allele- and tissue-specific. *Nat. Commun.* 12, 1808. <https://doi.org/10.1038/s41467-021-22125-z>.
37. Martincorena, I., Raine, K.M., Gerstung, M., Dawson, K.J., Haase, K., Van Loo, P., Davies, H., Stratton, M.R., and Campbell, P.J. (2017). Universal patterns of selection in cancer and somatic tissues. *Cell* 171, 1029–1041.e21. <https://doi.org/10.1016/j.cell.2017.09.042>.
38. Arnedo-Pac, C., Mularoni, L., Muiños, F., Gonzalez-Perez, A., and Lopez-Bigas, N. (2019). OncodriveCLUSTL: a sequence-based clustering method to identify cancer drivers. *Bioinformatics* 35, 4788–4790. <https://doi.org/10.1093/bioinformatics/btz501>.
39. Skoulidis, F., and Heymach, J.V. (2019). Co-occurring genomic alterations in non-small-cell lung cancer biology and therapy. *Nat. Rev. Cancer* 19, 495–509. <https://doi.org/10.1038/s41586-019-0179-8>.
40. Liu, P., Morrison, C., Wang, L., Xiong, D., Vedell, P., Cui, P., Hua, X., Ding, F., Lu, Y., James, M., et al. (2012). Identification of somatic mutations in non-small cell lung carcinomas using whole-exome sequencing. *Carcinogenesis* 33, 1270–1276. <https://doi.org/10.1093/carcin/bgs148>.
41. Nik-Zainal, S., Alexandrov, L.B., Wedge, D.C., Van Loo, P., Greenman, C.D., Raine, K., Jones, D., Hinton, J., Marshall, J., Stebbings, L.A., et al. (2012). Mutational processes molding the genomes of 21 breast cancers. *Cell* 149, 979–993. <https://doi.org/10.1016/j.cell.2012.04.024>.
42. Alexandrov, L.B., Nik-Zainal, S., Wedge, D.C., Aparicio, S.A.J.R., Behjati, S., Biankin, A.V., Bignell, G.R., Bolli, N., Borg, A., Børresen-Dale, A.L., et al. (2013). Signatures of mutational processes in human cancer. *Nature* 500, 415–421. <https://doi.org/10.1038/nature12477>.
43. Alexandrov, L.B., Ju, Y.S., Haase, K., Van Loo, P., Martincorena, I., Nik-Zainal, S., Totoki, Y., Fujimoto, A., Nakagawa, H., Shibata, T., et al. (2016). Mutational signatures associated with tobacco smoking in human cancer. *Science* 354, 618–622. <https://doi.org/10.1126/science.aag0299>.
44. Aftimos, P., Oliveira, M., Irrthum, A., Fumagalli, D., Sotiriou, C., Gal-Yam, E.N., Robson, M.E., Ndozeng, J., Di Leo, A., Ciruelos, E.M., et al. (2021). Genomic and transcriptomic analyses of breast cancer primaries and matched metastases in AURORA, the breast international group (BIG) molecular screening initiative. *Cancer Discov.* 11, 2796–2811. <https://doi.org/10.1158/2159-8290.CD-20-1647>.
45. Roberts, S.A., Lawrence, M.S., Klimczak, L.J., Grimm, S.A., Fargo, D., Stojanov, P., Kiezun, A., Kryukov, G.V., Carter, S.L., Saksena, G., et al. (2013). An APOBEC cytidine deaminase mutagenesis pattern is widespread in human cancers. *Nat. Genet.* 45, 970–976. <https://doi.org/10.1038/ng.2702>.
46. Taylor, B.J., Nik-Zainal, S., Wu, Y.L., Stebbings, L.A., Raine, K., Campbell, P.J., Rada, C., Stratton, M.R., and Neuberger, M.S. (2013). DNA deaminases induce break-associated mutation showers with implication of APOBEC3B and 3A in breast cancer kataegis. *Elife* 2, e00534. <https://doi.org/10.7554/eLife.00534>.
47. D'Antonio, M., Tamayo, P., Mesirov, J.P., and Frazer, K.A. (2016). Kataegis expression signature in breast cancer is associated with late onset, better prognosis, and higher HER2 levels. *Cell Rep.* 16, 672–683. <https://doi.org/10.1016/j.celrep.2016.06.026>.
48. Subramanian, A., Tamayo, P., Mootha, V.K., Mukherjee, S., Ebert, B.L., Gillette, M.A., Paulovich, A., Pomeroy, S.L., Golub, T.R., Lander, E.S., and Mesirov, J.P. (2005). Gene set enrichment analysis: a knowledge-based approach for interpreting genome-wide expression profiles. *Proc. Natl. Acad. Sci. USA* 102, 15545–15550. <https://doi.org/10.1073/pnas.0506580102>.
49. Liberzon, A., Birger, C., Thorvaldsdóttir, H., Ghandi, M., Mesirov, J.P., and Tamayo, P. (2015). The molecular signatures database hallmark gene set collection. *Cell Syst.* 1, 417–425. <https://doi.org/10.1016/j.cels.2015.12.004>.
50. Mosesson, Y., Mills, G.B., and Yarden, Y. (2008). Derailed endocytosis: an emerging feature of cancer. *Nat. Rev. Cancer* 8, 835–850. <https://doi.org/10.1038/nrc2521>.
51. Hanahan, D. (2022). Hallmarks of cancer: new dimensions. *Cancer Discov.* 12, 31–46. <https://doi.org/10.1158/2159-8290.CD-21-1059>.

52. Chen, Y., Zander, R.A., Wu, X., Schauder, D.M., Kasmani, M.Y., Shen, J., Zheng, S., Burns, R., Taparowsky, E.J., and Cui, W. (2021). BATF regulates progenitor to cytolytic effector CD8+ T cell transition during chronic viral infection. *Nat. Immunol.* 22, 996–1007. <https://doi.org/10.1038/s41590-021-00965-7>.
53. Seo, H., González-Avalos, E., Zhang, W., Ramchandani, P., Yang, C., Lio, C.-W.J., Rao, A., and Hogan, P.G. (2021). BATF and IRF4 cooperate to counter exhaustion in tumor-infiltrating CAR T cells. *Nat. Immunol.* 22, 983–995. <https://doi.org/10.1038/s41590-021-00964-8>.
54. Rice, C.M., Davies, L.C., Subleski, J.J., Maio, N., Gonzalez-Cotto, M., Andrews, C., Patel, N.L., Palmieri, E.M., Weiss, J.M., Lee, J.-M., et al. (2018). Tumour-elicited neutrophils engage mitochondrial metabolism to circumvent nutrient limitations and maintain immune suppression. *Nat. Commun.* 9, 5099. <https://doi.org/10.1038/s41467-018-07505-2>.
55. Tartey, S., Neale, G., Vogel, P., Malireddi, R.K.S., and Kanneganti, T.-D. (2021). A MyD88/IL1R Axis regulates PD-1 expression on tumor-associated macrophages and sustains their immunosuppressive function in melanoma. *Cancer Res.* 81, 2358–2372. <https://doi.org/10.1158/0008-5472.CAN-20-3510>.
56. Xia, C., Braunstein, Z., Toomey, A.C., Zhong, J., and Rao, X. (2017). S100 proteins as an important regulator of macrophage inflammation. *Front. Immunol.* 8, 1908.
57. Dufour, J.H., Dziejman, M., Liu, M.T., Leung, J.H., Lane, T.E., and Luster, A.D. (2002). IFN- γ -Inducible protein 10 (IP-10; CXCL10)-deficient mice reveal a role for IP-10 in effector T cell generation and trafficking. *J. Immunol.* 168, 3195–3204. <https://doi.org/10.4049/jimmunol.168.7.3195>.
58. Abd Hamid, M., Colin-York, H., Khalid-Alham, N., Browne, M., Cerundolo, L., Chen, J.-L., Yao, X., Rosendo-Machado, S., Waugh, C., Maldonado-Perez, D., et al. (2020). Self-maintaining CD103+ cancer-specific T cells are highly energetic with rapid cytotoxic and effector responses. *Cancer Immunol. Res.* 8, 203–216. <https://doi.org/10.1158/2326-6066.CIR-19-0554>.
59. Duhén, T., Duhén, R., Montler, R., Moses, J., Moudgil, T., de Miranda, N.F., Goodall, C.P., Blair, T.C., Fox, B.A., McDermott, J.E., et al. (2018). Co-expression of CD39 and CD103 identifies tumor-reactive CD8 T cells in human solid tumors. *Nat. Commun.* 9, 2724. <https://doi.org/10.1038/s41467-018-05072-0>.
60. Bancheau, R., Chitre, A.S., Scherl, A., Wu, T.D., Patil, N.S., de Almeida, P., Kadel III, E.E., Madireddi, S., Au-Yeung, A., Takahashi, C., et al. (2021). Intratumoral CD103+ CD8+ T cells predict response to PD-L1 blockade. *J. Immunother. Cancer* 9, e002231. <https://doi.org/10.1136/jitc-2020-002231>.
61. Andreatta, M., Corria-Osorio, J., Müller, S., Cubas, R., Coukos, G., and Carmona, S.J. (2021). Interpretation of T cell states from single-cell transcriptomics data using reference atlases. *Nat. Commun.* 12, 2965. <https://doi.org/10.1038/s41467-021-23324-4>.
62. Danaher, P., Warren, S., Dennis, L., D'Amico, L., White, A., Disis, M.L., Geller, M.A., Odunsi, K., Beechem, J., and Fling, S.P. (2017). Gene expression markers of tumor infiltrating leukocytes. *J. Immunother. Cancer* 5, 18. <https://doi.org/10.1186/s40425-017-0215-8>.
63. Brastianos, P.K., Kim, A.E., Wang, N., Lee, E.Q., Ligibel, J., Cohen, J.V., Chukwueke, U.N., Mahar, M., Oh, K., White, M.D., et al. (2021). Palbociclib demonstrates intracranial activity in progressive brain metastases harboring cyclin-dependent kinase pathway alterations. *Nat. Can. (Que.)* 2, 498–502. <https://doi.org/10.1038/s43018-021-00198-5>.
64. Doron, H., Pukrop, T., and Erez, N. (2019). A Blazing landscape: neuroinflammation shapes brain metastasis. *Cancer Res.* 79, 423–436. <https://doi.org/10.1158/0008-5472.CAN-18-1805>.
65. Samstein, R.M., Krishna, C., Ma, X., Pei, X., Lee, K.-W., Makarov, V., Kuo, F., Chung, J., Srivastava, R.M., Purohit, T.A., et al. (2021). Mutations in BRCA1 and BRCA2 differentially affect the tumor microenvironment and response to checkpoint blockade immunotherapy. *Nat. Can. (Que.)* 1, 1188–1203. <https://doi.org/10.1038/s43018-020-00139-8>.
66. Molgora, M., Esaurova, E., Vermi, W., Hou, J., Chen, Y., Luo, J., Brioschi, S., Bugatti, M., Omodei, A.S., Ricci, B., et al. (2020). TREM2 modulation remodels the tumor myeloid landscape enhancing anti-PD-1 immunotherapy. *Cell* 182, 886–900.e17. <https://doi.org/10.1016/j.cell.2020.07.013>.
67. McGranahan, N., Furness, A.J.S., Rosenthal, R., Ramskov, S., Lyngaa, R., Saini, S.K., Jamal-Hanjani, M., Wilson, G.A., Birkbak, N.J., Hiley, C.T., et al. (2016). Clonal neoantigens elicit T cell immunoreactivity and sensitivity to immune checkpoint blockade. *Science* 351, 1463–1469. <https://doi.org/10.1126/science.aaf1490>.
68. Rizvi, N.A., Hellmann, M.D., Snyder, A., Kvistborg, P., Makarov, V., Havel, J.J., Lee, W., Yuan, J., Wong, P., Ho, T.S., et al. (2015). Mutational landscape determines sensitivity to PD-1 blockade in non-small cell lung cancer. *Science* 348, 124–128. <https://doi.org/10.1126/science.aaa1348>.
69. Cosgrove, N., Vareslija, D., Keelan, S., Elangovan, A., Atkinson, J.M., Cocciglia, S., Bane, F.T., Singh, V., Furney, S., Hu, C., et al. (2022). Mapping molecular subtype specific alterations in breast cancer brain metastases identifies clinically relevant vulnerabilities. *Nat. Commun.* 13, 514. <https://doi.org/10.1038/s41467-022-27987-5>.
70. Reschke, R., Yu, J., Flood, B., Higgs, E.F., Hatogai, K., and Gajewski, T.F. (2021). Immune cell and tumor cell-derived CXCL10 is indicative of immunotherapy response in metastatic melanoma. *J. Immunother. Cancer* 9, e003521. <https://doi.org/10.1136/jitc-2021-003521>.
71. De Mattos-Arruda, L., Mayor, R., Ng, C.K.Y., Weigelt, B., Martínez-Ricarte, F., Torrejon, D., Oliveira, M., Arias, A., Raventos, C., Tang, J., et al. (2015). Cerebrospinal fluid-derived circulating tumour DNA better represents the genomic alterations of brain tumours than plasma. *Nat. Commun.* 6, 8839. <https://doi.org/10.1038/ncomms9839>.
72. Li, H., and Durbin, R. (2010). Fast and accurate long-read alignment with Burrows-Wheeler transform. *Bioinformatics* 26, 589–595. <https://doi.org/10.1093/bioinformatics/btp698>.
73. Talevich, E., Shain, A.H., Botton, T., and Bastian, B.C. (2016). CNVkit: genome-wide copy number detection and visualization from targeted DNA sequencing. *PLoS Comput. Biol.* 12, e1004873. <https://doi.org/10.1371/journal.pcbi.1004873>.
74. Bray, N.L., Pimentel, H., Melsted, P., and Pachter, L. (2016). Near-optimal probabilistic RNA-seq quantification. *Nat. Biotechnol.* 34, 525–527. <https://doi.org/10.1038/nbt.3519>.
75. Hundal, J., Kiwala, S., McMichael, J., Miller, C.A., Xia, H., Wollam, A.T., Liu, C.J., Zhao, S., Feng, Y.-Y., Graubert, A.P., et al. (2020). pVACtools: a computational toolkit to identify and visualize cancer neoantigens. *Cancer Immunol. Res.* 8, 409–420. <https://doi.org/10.1158/2326-6066.CIR-19-0401>.
76. Bankhead, P., Loughrey, M.B., Fernández, J.A., Dombrowski, Y., McArt, D.G., Dunne, P.D., McQuaid, S., Gray, R.T., Murray, L.J., Coleman, H.G., et al. (2017). QuPath: open source software for digital pathology image analysis. *Sci. Rep.* 7, 16878. <https://doi.org/10.1038/s41598-017-17204-5>.
77. Mayakonda, A., Lin, D.-C., Assenov, Y., Plass, C., and Koeffler, H.P. (2018). Maftools: efficient and comprehensive analysis of somatic variants in cancer. *Genome Res.* 28, 1747–1756. <https://doi.org/10.1101/gr.239244.118>.
78. Kuilman, T., Velds, A., Kemper, K., Ranzani, M., Bombardelli, L., Hoogstraal, M., Nevedomskaya, E., Xu, G., de Ruiter, J., Lolkema, M.P., et al. (2015). CopywriteR: DNA copy number detection from off-target sequence data. *Genome Biol.* 16, 49. <https://doi.org/10.1186/s13059-015-0617-1>.
79. Miller, C.A., White, B.S., Dees, N.D., Griffith, M., Welch, J.S., Griffith, O.L., Vij, R., Tomasson, M.H., Graubert, T.A., Walter, M.J., et al. (2014). SciClone: inferring clonal architecture and tracking the spatial and temporal patterns of tumor evolution. *PLoS Comput. Biol.* 10, e1003665. <https://doi.org/10.1371/journal.pcbi.1003665>.

80. Love, M.I., Huber, W., and Anders, S. (2014). Moderated estimation of fold change and dispersion for RNA-seq data with DESeq2. *Genome Biol.* *15*, 550. <https://doi.org/10.1186/s13059-014-0550-8>.
81. Schmidt, U., Weigert, M., Broaddus, C., and Myers, G. (2018). Cell detection with star-convex polygons. In *Medical Image Computing and Computer Assisted Intervention – MICCAI 2018 Lecture Notes in Computer Science*, A.F. Frangi, J.A. Schnabel, C. Davatzikos, C. Alberola-López, and G. Fichtinger, eds. (Springer International Publishing), pp. 265–273. https://doi.org/10.1007/978-3-030-00934-2_30.
82. Cibulskis, K., Lawrence, M.S., Carter, S.L., Sivachenko, A., Jaffe, D., Sougnez, C., Gabriel, S., Meyerson, M., Lander, E.S., and Getz, G. (2013). Sensitive detection of somatic point mutations in impure and heterogeneous cancer samples. *Nat. Biotechnol.* *31*, 213–219. <https://doi.org/10.1038/nbt.2514>.
83. Chen, X., Schulz-Trieglaff, O., Shaw, R., Barnes, B., Schlesinger, F., Källberg, M., Cox, A.J., Kruglyak, S., and Saunders, C.T. (2016). Manta: rapid detection of structural variants and indels for germline and cancer sequencing applications. *Bioinformatics* *32*, 1220–1222. <https://doi.org/10.1093/bioinformatics/btv710>.
84. Lee, J., Lee, A.J., Lee, J.-K., Park, J., Kwon, Y., Park, S., Chun, H., Ju, Y.S., and Hong, D. (2018). Mutalisk: a web-based somatic MUTation AnaLYS toolKit for genomic, transcriptional and epigenomic signatures. *Nucleic Acids Res.* *46*, W102–W108. <https://doi.org/10.1093/nar/gky406>.
85. Shukla, S.A., Rooney, M.S., Rajasagi, M., Tiao, G., Dixon, P.M., Lawrence, M.S., Stevens, J., Lane, W.J., Dellagatta, J.L., Steelman, S., et al. (2015). Comprehensive analysis of cancer-associated somatic mutations in class I HLA genes. *Nat. Biotechnol.* *33*, 1152–1158. <https://doi.org/10.1038/nbt.3344>.
86. Wu, T., Hu, E., Xu, S., Chen, M., Guo, P., Dai, Z., Feng, T., Zhou, L., Tang, W., Zhan, L., et al. (2021). clusterProfiler 4.0: a universal enrichment tool for interpreting omics data. *Innovation* *2*, 100141. <https://doi.org/10.1016/j.xinn.2021.100141>.
87. Skidmore, Z.L., Wagner, A.H., Lesurf, R., Campbell, K.M., Kunisaki, J., Griffith, O.L., and Griffith, M. (2016). GenVisR: genomic visualizations in R. *Bioinformatics* *32*, 3012–3014. <https://doi.org/10.1093/bioinformatics/btw325>.
88. Krzywinski, M., Schein, J., Birol, Ì., Connors, J., Gascoyne, R., Horsman, D., Jones, S.J., and Marra, M.A. (2009). Circos: an information aesthetic for comparative genomics. *Genome Res.* *19*, 1639–1645. <https://doi.org/10.1101/gr.092759.109>.

STAR★METHODS

KEY RESOURCES TABLE

REAGENT or RESOURCE	SOURCE	IDENTIFIER
Antibodies		
AF700 mouse monoclonal anti-human CD45 (clone HI30)	BioLegend	Cat#304024; RRID:AB_493761
BV421 rat monoclonal anti-mouse/human CD11B (clone M1/70)	BioLegend	Cat#101251; RRID:AB_2562904
PE mouse monoclonal anti-human CD66B (clone G10F5)	BioLegend	Cat#305106; RRID:AB_2077857
PE mouse monoclonal anti-human CD66B (clone 6/40C)	BioLegend	Cat#392904; RRID:AB_2750202
AF488 mouse monoclonal anti-human CD14 (clone HCD14)	BioLegend	Cat#325610; RRID:AB_830683
BUV737 mouse monoclonal anti-human CD16 (clone 3G8)	BD	Cat#612786; RRID:AB_2833077
APC mouse monoclonal anti-human CD49D (clone 9F10)	BioLegend	Cat#304308; RRID:AB_2130041
BV605 mouse monoclonal anti-human CD11C (clone 3.9)	BioLegend	Cat#301636; RRID:AB_2563796
BV711 mouse monoclonal anti-human HLA-DR (clone L243)	BioLegend	Cat#307644; RRID:AB_2562913
PerCP/Cy5.5 mouse monoclonal anti-human CD3 (clone HIT3a)	BioLegend	Cat#300328; RRID:AB_1575008
BV650 mouse monoclonal anti-human CD4 (clone OKT4)	BioLegend	Cat#317436; RRID:AB_2563050
PE mouse monoclonal anti-human CD25 (clone BC96)	BioLegend	Cat#302606; RRID:AB_314276
BV510 mouse monoclonal anti-human CD127 (clone A019D5)	BioLegend	Cat#351332; RRID:AB_2562304
PE/Cy7 mouse monoclonal anti-human CD8A (clone HIT8a)	BioLegend	Cat#300914; RRID:AB_314118
BUV563 mouse monoclonal anti-human CD20 (clone 2H7)	BD	Cat#748456; RRID:AB_2872872
BUV563 mouse monoclonal anti-human CD19 (clone SJ25C1)	BD	Cat#612916; RRID:AB_2870201
PE/Dazzle mouse monoclonal anti-human CD56 (clone HDC56)	BioLegend	Cat#318348; RRID:AB_2563564
PE mouse monoclonal anti-human P2RY12 (clone S16001E)	BioLegend	Cat# 392104; RRID:AB_2716007
PE/Cy7 mouse monoclonal anti-human CD68 (clone Y1/82A)	BioLegend	Cat#333816; RRID:AB_2562936
Goat polyclonal anti-human CD45 (IF, 1:100 dilution)	LSBio	Cat#LS-B14248-300; RRID:AB_2889893
Mouse monoclonal anti-human CD8 (clone 4B11) (IF, 1:100 dilution)	Bio-Rad	Cat# MCA1817; RRID:AB_322868
Rabbit monoclonal anti-human CD4 (clone EPR6855) (IF, 1:50 dilution)	Abcam	Cat#ab133616; AB_2750883
Mouse monoclonal anti-human CD15 (clone MMA) (IF, 1:100 dilution)	Abcam	Cat#ab17080; AB_443635

(Continued on next page)

Continued

REAGENT or RESOURCE	SOURCE	IDENTIFIER
Rabbit monoclonal anti-human CD103 (clone EPR22590-27) (IF, 1:100 dilution)	Abcam	Cat#ab224202; AB_2891141
AF555 donkey anti-mouse IgG (1:500 dilution)	ThermoFisher	Cat#A32773; RRID:AB_2762848
AF647 donkey anti-rabbit IgG (1:500 dilution)	Invitrogen	Cat#A31573; RRID: AB_2536183
DyLight755 donkey anti-goat IgG (1:500 dilution)	Invitrogen	Cat# SA5-10091; RRID:AB_2556671
DAPI (1 µg/mL)	Invitrogen	Cat#D1306; RRID:AB_2629482
Biological samples		
Human brain metastasis tissue	Centre Hospitalier Universitaire Vaudois, Lausanne, Switzerland	N/A
Human blood	Centre Hospitalier Universitaire Vaudois, Lausanne, Switzerland	N/A
Chemicals, peptides, and recombinant proteins		
Trizol LS	Thermo Fisher	Cat#10296028
Tween 20	Applied Chemicals	Cat#A4974
Triton X-100	Applied Chemicals	Cat#A4975
Fluorescence Mounting Medium	Dako	Cat#S302380
Critical commercial assays		
Tumor Dissociation Kit, human	Miltenyi	Cat#130-095-929
Human TruStain FcX	BioLegend	Cat#422302
ZombieNIR Fixable Viability Kit	BioLegend	Cat#423106
Qiagen DNaseasy Blood & Tissue kit	Qiagen	Cat#69504
Deposited data		
RNA-Seq count data	This paper	https://joycelab.shinyapps.io/braintime/
Human reference genome, hg38 (GRCh38.95, Jan 2019)	EMBL/EBI	http://jan2019.archive.ensembl.org/index.html
TCGA datasets	Genomics Data Common	https://portal.gdc.cancer.gov/
Molecular Signatures Database gene set collection	UC San Diego and Broad Institute	https://www.gsea-msigdb.org/gsea/msigdb/
The Gene Ontology Resource	Gene Ontology Consortium	http://geneontology.org/
Software and algorithms		
FastQC (version 0.11.7)	Babraham Institute	https://www.bioinformatics.babraham.ac.uk/projects/fastqc/
Cutadapt (version 2.3)	National Bioinformatics Infrastructure Sweden	https://cutadapt.readthedocs.io/en/stable/
Burrows-Wheeler Aligner (version 0.7.17)	Li and Durbin ⁷²	http://bio-bwa.sourceforge.net/
GATK (version 4.1.0.0)	Broad Institute	https://gatk.broadinstitute.org/hc/en-us
Samtools (version 1.8)	Genome Research Limited	http://www.htslib.org/
Picard tools (version 2.9.0)	Broad Institute	https://broadinstitute.github.io/picard/
Vcftools (version 0.1.16)	Adam Auton, Petr Danecek, Anthony Marcketta	https://vcftools.github.io/index.html
Variant Effect Predictor (version 95)	EMBL/EBI	https://github.com/Ensembl/ensembl-vep
CNVKit (version 0.9.10)	Talevich et al. ⁷³	https://cnvkit.readthedocs.io/en/stable/
Manta (version 1.6.0)	Illumina	https://github.com/Illumina/manta
Kallisto (version 0.46.0)	Bray et al. ⁷⁴	https://pachterlab.github.io/kallisto/

(Continued on next page)

Continued

REAGENT or RESOURCE	SOURCE	IDENTIFIER
Polysolver (version 4.0–1)	Broad Institute	https://software.broadinstitute.org/cancer/cga/polysolver
Pvactools (version 2.0.0)	Hundal et al. ⁷⁵	https://pvactools.readthedocs.io/en/latest/
GNU bash (version 3.2.57)	GNU Project	https://www.gnu.org/software/bash/
GNU coreutils (version 9.0)	GNU project	https://www.gnu.org/software/coreutils/
Docker (version 20.10.5)	Docker, Inc	https://www.docker.com/
GraphPad Prism (version 9.1.1)	GraphPad software	https://www.graphpad.com/scientific-software/prism/
FlowJo (version 10.5.3)	BD Biosciences	https://www.flowjo.com/
R (version 4.1.0)	The R Foundation	https://cran.r-project.org/
OncodriveCLUSTL (version 1.1.4)	Arnedo-Pac et al. ³⁸	https://bitbucket.org/bbgjlab/oncodriveclustl/src/master/
MUSCLE (version 3.8.31)	EMBL-EBI	https://www.ebi.ac.uk/Tools/msa/muscle/
Chimera (version 1.13.1)	University of California San Francisco (UCSF)	https://www.cgl.ucsf.edu/chimera/
QuPath (version 0.3.0)	Bankhead et al. ⁷⁶	https://qupath.github.io/
dNdScv (R package, version 0.1.0)	Martincorena et al. ³⁷	https://github.com/im3sanger/dndscv
MAFtools (R package, version 2.8.0)	Mayakonda et al. ⁷⁷	https://www.bioconductor.org/packages/release/bioc/html/maftools.html
CopyWriteR (R package, version 2.24.0)	Kuilman et al. ⁷⁸	https://www.bioconductor.org/packages/release/bioc/html/CopywriteR.html
SciClone (R package, version 1.1.0)	Miller et al. ⁷⁹	https://github.com/genome/sciclone
DESeq2 (R package, version 1.32.0)	Love et al. ⁸⁰	https://www.bioconductor.org/packages/release/bioc/html/DESeq2.html
Ggplot2 (R package, version 3.3.35)	Hadley Wickham	https://ggplot2.tidyverse.org/
Stats (R package, version 4.1.0)	The R Foundation	https://cran.r-project.org/
Tximport (R package, version 1.20.0)	Bioconductor	https://www.bioconductor.org/packages/release/bioc/html/tximport.html
EnsemblDb (R package, version 2.16.0)	Bioconductor	https://www.bioconductor.org/packages/release/bioc/html/ensemldb.html
AnnotationHub (R package, version 3.0.1)	Bioconductor	https://www.bioconductor.org/packages/release/bioc/html/AnnotationHub.html
RColorBrewer (R package, version 1.1–2)	The Comprehensive R Archive Network (CRAN)	https://cran.r-project.org/web/packages/RColorBrewer/index.html
GSVA (R package, version 1.40.1)	Bioconductor	https://www.bioconductor.org/packages/release/bioc/html/GSVA.html
Pheatmap (R package, version 1.0.12)	The Comprehensive R Archive Network (CRAN)	https://cran.r-project.org/web/packages/pheatmap/index.html
UpSetR (R package, version 1.4.0)	The Comprehensive R Archive Network (CRAN)	https://cran.r-project.org/web/packages/UpSetR/index.html
Dplyr (R package, version 1.0.7)	Hadley Wickham	https://dplyr.tidyverse.org/
Reshape2 (R package, version 1.4.4)	The Comprehensive R Archive Network (CRAN)	https://cran.r-project.org/web/packages/reshape2/index.html
Scales (R package, version 1.1.1)	The Comprehensive R Archive Network (CRAN)	https://scales.r-lib.org/
Ggpubr (R package, version 0.4.0)	The Comprehensive R Archive Network (CRAN)	https://cran.r-project.org/web/packages/ggpubr/index.html
EDASeq (R package, version 2.26.1)	Bioconductor	https://www.bioconductor.org/packages/release/bioc/html/EDASeq.html

(Continued on next page)

Continued

REAGENT or RESOURCE	SOURCE	IDENTIFIER
org.Hs.eg.db (R package, version 3.13.0)	Bioconductor	https://www.bioconductor.org/packages/release/data/annotation/html/org.Hs.eg.db.html
ClusterProfiler (R package, version 4.0.0)	Bioconductor	https://www.bioconductor.org/packages/release/bioc/html/clusterProfiler.html
Gprofiler2 (R package, version 0.2.0)	The Comprehensive R Archive Network (CRAN)	https://cran.r-project.org/web/packages/gprofiler2/index.html
GenVisR (R package, version 1.24.0)	Bioconductor	https://bioconductor.org/packages/release/bioc/html/GenVisR.html

Other

gentleMACS Octo Dissociator with heaters	Miltenyi	Cat# 130-096-427
gentleMACS C Tubes	Miltenyi	Cat#130-096-334
LSR II flow cytometer	BD	N/A
Fortessa flow cytometer	BD	N/A
FACSAria III, flow cytometer and cell sorter	BD	N/A
FACSAria II SORP, flow cytometer and cell sorter	BD	N/A
Axio Scan.Z1 slide scanner	Zeiss	N/A
NanoDrop One spectrophotometer	ThermoFisher	Cat# ND-ONEC-W
Qubit fluorometer	Invitrogen, ThermoFisher	Cat# Q33238
TissueLyser II	Qiagen	Cat #85300

RESOURCE AVAILABILITY

Lead contact

Further information and requests for resources should be directed to the lead contact, Prof. Johanna A. Joyce (johanna.joyce@unil.ch).

Materials availability

This study did not generate new, unique reagents.

Data and code availability

RNA-seq count expression data generated during this study can currently be accessed and visualized at:

<https://joycelab.shinyapps.io/braintime/>

Due to strict patient privacy protection, requests for access to the raw DNA and RNA-seq data must be made to the **lead contact** for subsequent referral to the institutional ethics committee. Data reported in this paper is available from the **lead contact**. Software used in this manuscript are listed in the **key resources table**. This paper does not report original code. Any additional information required to reanalyze the data reported in this paper is available from the **lead contact** upon request.

EXPERIMENTAL MODEL AND SUBJECT DETAILS

All experimental procedures performed on clinical tissue samples obtained from human participants were in accordance with the ethical standards of the institutional and/or national research committees, and with the 1964 Helsinki declaration and its later amendments or comparable ethical standards. Informed consent was obtained from all individual participants included in this study. The collection of tumor tissue and blood samples at the Biobank of the Brain and Spine Tumor Center (BB_031_BBLBGT) of the Center Hospitalier Universitaire Vaudois (CHUV, Lausanne, Switzerland) was approved by the Commission Cantonale d'éthique de la recherche sur l'être humain (CER-VD, protocol PB 2017-00240, F25/99). Tissue specimens were immediately collected from the operating room and processed as described below. All samples were fully anonymized before any processing/experimentation. Pathological review of tumor tissues was performed at CHUV as part of the standard clinical care; all clinical information is included in **Table S1A**. Clinical information referring to 'sex' was evaluated and reported in the medical history of the patients by their physicians.

METHOD DETAILS

Clinical sample processing, flow cytometry, fluorescence-activated cell sorting, immunofluorescence, DNA sequencing and RNA sequencing of sorted populations

Clinical sample processing and preparation for flow cytometry (FCM), fluorescence-activated cell sorting (FACS), immunofluorescence (IF) staining, RNA sequencing of sorted populations (RNA-seq), whole-exome sequencing (WES) and low-pass whole-genome sequencing (LP-WGS) was performed as described in modules 2a (FCM, FACS), 1a (IF), 1b (WES, LP-WGS) and 2b (RNA-seq), respectively.³³

Flow cytometry markers and definition of cell populations for fluorescence-activated cell sorting

The following markers were used to define immune and non-immune cell populations for the quantifications shown in Figures 3A, 3B, 5A, and 5B and for cell sorting:

Cell population	Markers
CD45-negative	CD45 ⁻
Lymphocytes	CD45 ⁺ , CD11B ⁻
Myeloid cells	CD45 ⁺ , CD11B ⁺
Monocyte-derived macrophages (MDM)	CD45 ⁺ , CD11B ⁺ , CD66B ⁻ , CD14 ⁺ , CD16 ⁻ , CD49D ^{high}
Microglia	CD45 ⁺ , CD11B ⁺ , CD66B ⁻ , CD14 ⁺ , CD16 ⁻ , CD49D ^{low}
Neutrophils	CD45 ⁺ , CD11B ⁺ , CD66B ⁺ , CD16 ⁺
B cells	CD45 ⁺ , CD11B ⁻ , CD19 ⁺ , CD3 ⁻
Dendritic cells (DC)	CD45 ⁺ , CD11B ⁺ , CD66B ⁻ , CD14 ^{low} , CD16 ⁻ , CD49D ^{med} , HLA-DR ⁺ , CD11C ⁺
NK cells	CD45 ⁺ , CD11B ⁻ , CD19 ⁻ , CD3 ⁻ , CD56 ⁺
CD8 ⁺ T cells	CD45 ⁺ , CD11B ⁻ , CD19 ⁻ , CD3 ⁺ , CD4 ⁻ , CD8 ⁺
CD4 ⁺ T cells	CD45 ⁺ , CD11B ⁻ , CD19 ⁻ , CD3 ⁺ , CD4 ⁺ , CD8 ⁻ , CD25 ⁻
Regulatory T cells (Treg)	CD45 ⁺ , CD11B ⁻ , CD19 ⁻ , CD3 ⁺ , CD4 ⁺ , CD8 ⁻ , CD127 ^{low} , CD25 ⁺
Double-negative (DN) T cells	CD45 ⁺ , CD11B ⁻ , CD19 ⁻ , CD3 ⁺ , CD4 ⁻ , CD8 ⁻
CD16 neg. granulocytes	CD45 ⁺ , CD11B ⁺ , CD66B ⁺ , CD16 ⁻
CD14 ^{-/low} /CD16 ⁺ monocytes	CD45 ⁺ , CD11B ⁺ , CD66B ⁻ , CD14 ^{-/low} , CD16 ⁺
CD14 ⁺ /CD16 ⁺ monocytes	CD45 ⁺ , CD11B ⁺ , CD66B ⁻ , CD14 ⁺ , CD16 ⁺
Immature myeloid cells (iMC)	CD45 ⁺ , CD11B ⁺ , CD66B ⁻ , CD14 ^{low} , CD16 ⁻ , CD49D ^{med} , HLA-DR ⁻ , CD11C ⁻

RNA-sequencing of sorted immune cell populations

2,000 cells of each of the following cell populations were sorted into Trizol LS as indicated in module 2b³³ and submitted to the company “GeneWiz from Azenta Life Sciences” for RNA extraction, quality control check, library preparation and RNA-seq: CD45-negative, microglia, MDM, neutrophils, CD8⁺ T cells and CD4⁺ T cells. Total RNA was extracted from cells following the Trizol Reagent User Guide (Thermo Fisher Scientific). Extracted RNA samples were quantified using Qubit 2.0 Fluorometer (Life Technologies, Carlsbad, CA, USA) and RNA integrity was assessed using Agilent TapeStation 4200 (Agilent Technologies, Palo Alto, CA, USA). SMART-Seq HT Ultra Low Input Kit for Sequencing was used for full-length cDNA synthesis and amplification (Clontech, Mountain View, CA), and Illumina Nextera XT library was used for the sequencing library preparation, following the manufacturer’s instructions. Paired-end 150 base-pair (2 × 150) sequencing of the libraries was performed using an Illumina NovaSeq 6000 sequencer.

Bulk RNA-sequencing of validation cohort samples

17 of 18 tumor samples from the validation cohort had sufficient tissue to perform bulk RNA sequencing. Snap-frozen tumor tissue (~1–3 mm³ piece) was placed into a microcentrifuge tube containing 600μL lysis buffer (buffer RLT, Qiagen) and 5mm stainless steel

beads; disrupted and homogenized using a Tissue Lyser II system (Qiagen) at a frequency of 20Hz for 2 min. Total RNA was isolated using an RNAeasy Mini kit (Qiagen) following the manufacturer's instructions. Purified RNA was submitted to the Genewiz company ($\geq 2\mu\text{g}$ RNA per tumor at $\geq 20\text{ ng}/\mu\text{L}$; A260/A280 = 1.8–2.0 and DNA-free) for library preparation and RNA-seq, as detailed in the section "RNA-sequencing of sorted immune cell populations" above.

Whole-exome and low-pass whole-genome sequencing

Genomic DNA was isolated as indicated in module 1b³³ and submitted to the Genewiz company ($\geq 1.5\mu\text{g}$ DNA per tumor at $\geq 20\text{ ng}/\mu\text{L}$; A260/A280 = 1.8–2.0 and RNA-free) for library preparation and sequencing. The following quality control checks were performed for all samples before sequencing: (i) genomic DNA integrity assessment by gel electrophoresis and quantification of total concentration by Qubit assay; (ii) sonication efficiency and library size assessment by capillary electrophoresis using the 5300 Fragment Analyzer system (Agilent); (iii) quantification of library concentration by Qubit assay. Whole-exome and low-pass whole-genome sequencing libraries were generated using the SureSelect Human All Exon v7 kit (Agilent) and SureSelectQXT Library Prep (Agilent), respectively, following the manufacturer's instructions. Paired-end 150 base-pair (2×150) sequencing of the libraries was performed using an Illumina NovaSeq 6000 sequencer.

Immunofluorescence (IF) staining and quantification

Tissue processing and staining was performed as described in module 1a (IF),³³ except for the fixation, which was performed using 10% neutral-buffered formalin instead of methanol. Image quantification was performed using the QuPath 0.3.0⁷⁶ image analysis software. For each sample, a region of interest (ROI) was manually defined to exclude aberrant signals (i.e. those resulting from dust particles, tissue folds or air bubbles). Nuclear segmentation was performed using the StarDist method⁸¹ powered by the *dsb2018_heavy_augment.pb* deep learning model with the following parameters: threshold = 0.5; channels = 'DAPI'; pixelSize = 0; cellExpansion = 3; cellConstrainScale = 1.5; measureShape = true; measureIntensity = true; includeProbability = true; nThreads = 10. Classifiers for each marker/fluorophore were created by setting detection thresholds in a *per sample* basis. The ratio of false positive (FP) vs. true positive (TP) signal was calculated for each sample by dividing the number of positive cells for a given marker in the secondary-only control by the number of positive cells for the same marker in the fully stained tissue (primary plus secondary antibodies). Samples with an FP/TP $>2\%$ were excluded from the analyses.

Computational analyses

Somatic variant calling from WES data

Somatic variant calling was performed from WES data of paired tumor and PBMC samples. Raw reads (*fastq* files) were quality-control checked by FastQC and sequencing adaptors were removed by cutadapt. The resulting reads were then aligned to the hg38 (GRCh38.95) reference genome by using the Burrows-Wheeler aligner⁷² (command line: `bwa mem -M -t 64 -v 3 -R`). Aligned reads were sorted and written into BAM alignment files using SAMtools and marked for duplicates using Picard tools (command line: `picard-tools MarkDuplicates VALIDATION_STRINGENCY = LENIENT`). Somatic mutation calling was performed using MuTect2,⁸² GenomeAnalysisTK-4.0 (GATK4.0) and GATK Resource Bundle GRCh38 following best practices for somatic variant calling as described by The Broad Institute (<https://gatk.broadinstitute.org/hc/en-us/articles/360035894731-Somatic-short-variant-discovery-SNVs-Indels>): 1) Base quality scores were recalibrated using the GenomeAnalysisTK BaseRecalibrator function and "dbSNP v146" and "Mills and 1000 genomes" gold standard vcf files from the GATK resource bundle; 2) A panel of normal (PoN) was generated by running Mutect2 in tumor-only mode (parameters: `--disable-read-filter MateOnSameContigOrNoMappedMateReadFilter`) on individual PBMC samples and merging them using GenomeAnalysisTK CreateSomaticPanelOfNormals function into a single VCF file; 3) Somatic variants were called on recalibrated BAM files and written into VCF files (one per tumor sample) using MuTect2, the PoN generated in the previous step and GNOMAD (hg38) as the population germline variant resource (parameters: `--af-of-alleles-not-in-resource 0.0000025 --disable-read-filter MateOnSameContigOrNoMappedMateReadFilter`); 4) Cross-sample contamination was estimated using GenomeAnalysisTK GetPileupSummaries and GenomeAnalysisTK CalculateContamination functions; 5) Somatic variants were filtered to keep only confident calls by using the GenomeAnalysisTK FilterMutectCalls function provided with the contamination tables generated in step 4, the VCF files generated in step 3 and run with default parameters. Note that this step applies 14 different filters, details on filters/thresholds can be found in GATK4 documentation; 6) VCF files containing only "PASS" (filtered) variants were generated by using GenomeAnalysisTK SelectVariants (parameters: `--exclude-filtered`); 7) Filtered variants were annotated using ENSEMBL Variant Effect Predictor (VEP). See also "Software versions" table below.

Germline variant calling from WES data

Germline variant calling was performed using the Haplo-type Caller from GATK4.0 (GenomeAnalysisTK HaploTypeCaller `--disable-read-filter MateOnSameContigOrNoMappedMateReadFilter`) on recalibrated BAM files from PBMC samples as generated in step 1 of the somatic variant calling procedure described above.

Copy number variation (CNV) analysis from WES data

Copy number variation analysis was performed using CopyWriteR, which implements a statistical method to estimate CNV from off-target reads in capture-based sequencing experiments and overcomes most of the limitations and biases associated with CNV quantification from whole-exome sequencing data (see⁷⁸ for details). Briefly, the software processes the alignment files to remove non-random off-target reads, computes depth of coverage in predefined bins, corrects depth by GC content and mappability

and generates a CNV profile. On-target and off-target regions were identified based on germline (PBMC) samples, as recommended by the authors of the tool. We defined 20Kb bins and analyzed paired tumor and healthy tissue (PBMC -as a negative control-) samples, so that all copy number estimations reported for the tumor samples in this study are relative to their corresponding healthy control.

Copy number variation (CNV) imputation from LP-WGS data

CNV imputation from LP-WGS data was provided by GeneWiz (Azenta Life Sciences, Germany) via partnering with Gencove Inc (New York, United States). Briefly, reads were mapped to the Human GRCh38 genome using the Burrows-Wheeler aligner and CNV calling was performed using CNVkit⁷³ in wgs mode. The imputation panel used here corresponds to a lifted-over version (from GRCh37 to GRCh38) of the phased release of genotype calls from the New York Genome Center's resequencing of individuals from the 1000 Genomes Project. The panel is composed of 3202 individuals including the original 2504 from Phase 3 and an additional 798 relatives.

Structural variation (SV) analysis from WES data

Raw reads from paired tumor and healthy control (PBMC) samples were processed and aligned to the human genome (GRCh38.p12 v95 Jan 2019) as described in section "Somatic variant calling from WES data". Gene fusions/translocations were identified using manta⁸³ as follows: 1) Configure the analysis by executing configManta.py with parameters: -exome (indicates that reads come from a whole-exome sequencing experiment), -normalBam and -tumorBam (to define normal and tumor samples, respectively), -referenceFasta (to indicate genome of reference used for the alignment) -runDir (to define working directory); 2) Run the analysis by executing runWorkflow.py. Both configManta.py and runWorkflow.py are part of the standard manta distribution and can be downloaded from the link indicated in the section "Software versions".

Mutational signature deconvolution

Mutational signatures (COSMIC v3.2) were deconvoluted from WES data using Mutalisk⁸⁴ on VCF files containing filtered, high-quality single nucleotide variants (SNVs) generated as detailed in "Somatic variant calling from WES data" section. Maximum Likelihood Estimation (MLE) method was set to linear regression.

In silico cancer driver gene analysis

Cancer driver discovery analyses were performed on WES data using two independent approaches: (i) dN/dS method (dNdScv R package), which infers cancer driver genes (genes under positive selection) based on the ratio between non-synonymous and synonymous mutations.⁴³ A reference file for the human genome version GRCh38.p12 v95 was generated using the buildref function and subsequently employed to run driver discovery analysis by means of the dNdScv function, an implementation of the dN/dS method that combines local (synonymous mutations in each analyzed gene) and global (variation of the mutation rate across all analyzed genes) information to estimate background mutation and improves traditional dN/dS implementations. (ii) OncoDriveCLUSTL method,³⁸ which detects significant mutation clustering signals by comparing observed mutations to a simulated local background model of the distribution of mutations in the cohort under study. Driver detection was performed on all CDS regions (GRCh38.p12 v95) by executing oncodriverclustl with the following parameters: -smooth-window 11 -cluster-window 11 -kmer 3 -n-simulations 1000 -simulation-window 31 -simulation-mode mutation_centered -concatenate.

In silico saturation mutagenesis (BoostDM)

Predictions of TP53 driver and passenger mutations were performed by using BoostDM³⁴ and downloaded from the Integrative Onco Genomics (IntOGen) web service (<https://www.intogen.org/>) release 2020-02-01 (TCGA data). Lollipop plots included in Figure S1A were adapted from those downloaded from the IntOGen webpage.

Intratumor heterogeneity (ITH)

ITH was estimated using the R package SciClone,⁷⁹ which implements a Bayesian inference model to assign SNVs to clonality clusters based on variant allele frequencies (VAF). Clonal architecture was inferred from copy number neutral (diploid) genomic regions and only somatic variants (as identified in section "Somatic variant calling from WES data") supported by at least 50 reads ("Immunogenomics cohort", 9/9 breast-BrMs; 18/21 lung-BrMs) or 100 reads ("Validation cohort", 9/13 breast-BrMs; 5/5 lung-BrMs) were considered for the analyses. These thresholds were defined so that ITH could be reliably estimated in at least 50% of the samples from each primary tumor in each of the two cohorts. For each BrM tumor, variants belonging to the cluster with the highest VAF were annotated as "clonal", whereas those belonging to clusters with a lower VAF were annotated as "subclonal". ITH was estimated by computing the ratio of "subclonal" versus "clonal" variants, with higher ratios indicating a higher proportion of "subclonal" variants within the tumor cell population and therefore a higher ITH.

Mutual exclusivity and co-occurrence

Mutual exclusivity and co-occurrence analyses were performed with the MAFtools⁷⁷ built-in function somaticInteractions.

Molecular modeling predictions

Structural analysis of TP53 mutations were performed using crystallographic structures retrieved from the PDB (<https://www.rcsb.org/>), with PDB codes 1gzh, 1kzy, 1tsr, 1tup, 3kmd. Sequences of human TP53 and orthologs were retrieved from the UniProt database (<https://www.uniprot.org/>) and the alignment of the sequences was performed using MUSCLE. Structures shown in Figure S1C were performed using USCF Chimera.

Neoantigen prediction

Class I HLA typing was performed by using polysolver⁸⁵ on WES data from PBMC samples (command line: polysolver shell_call_hla_type (sorted bamfile) Unknown 1 hg38 ILM1.8 0 (output file)) and all haplotypes were summarized in a pVACtools⁷⁵ compatible text file via custom scripting. For each tumor sample, a VCF file containing confident somatic calls was generated as indicated in

“Somatic variant calling from WES data” section (steps 3–6) and annotated using the Variant Effect Predictor (VEP) with the Frameshift and Wildtype plugins (https://github.com/griffithlab/pVACtools/tree/master/tools/pvacseq/VEP_plugins) from the pVACtools team with the following parameters: `–cache_version 95 –dir_cache (vep cache folder) –species homo_sapiens –format vcf –vcf –symbol –terms SO –tsl –hgvs –fasta (GRCh38.95 fasta file) –plugin Frameshift –plugin Wildtype –output_file (VCF file)`. These annotated VCF files were further annotated with transcript expression information using VAtools (`vcf-expression-annotator` function) and used for neoantigen predictions. Neoantigens were predicted using a Docker containerized version of pVACtools (DockerHub: [griffithlab/pvactools:2.0.0](https://hub.docker.com/r/griffithlab/pvactools)). Briefly, we used the `pvaseq run` function to perform MHC-peptide binding affinity predictions with three MHC class I prediction algorithms (MHCflurry, MHCnuggetsI and NetMHC) for 8, 9 and 10-mer peptides. The following filters were applied to all identified neo-epitopes: (i) binding filter, to remove neoantigen candidates that do not meet desired peptide:MHC binding criteria. Threshold: median MT IC50 score + median fold change (mut vs. WT); (ii) coverage filter, to remove variants that do not meet desired read count and VAF criteria (in normal DNA and tumor DNA/RNA). Threshold: median MT IC50 score + median fold change (mut vs. WT); (iii) Transcript support level filter, to remove variant annotations based on low quality transcript annotations. Threshold: TSL = 1 (Highest level; ENSEMBL definition: “all splice junctions of the transcript are supported by at least one non-suspect mRNA”); (iv) top score filter. Threshold: median MT IC50 binding score of all chosen prediction methods. See also [Table S7](#).

Kataegis

Detection of hypermutated (kataegic) genomic regions was performed using the MAFtools⁷⁷ built-in function `rainfallPlot`. Genomic regions containing six or more mutations with an average inter-mutation distance ≤ 1000 base pairs were considered as kataegic.

Differential RNA-seq gene expression analysis

Reads were quality-checked by FastQC. Transcript quantification was performed using kallisto⁷⁴ and the hg38 (GRCh38.95) reference coding transcriptome (kallisto compatible indexes and quantifications were generated with the kallisto index and kallisto quant functions, respectively). Transcript-level quantifications were collapsed into gene quantifications using the R package `tximport` and an RNA transcript to gene mapping table containing mappings for all protein-coding genes. A raw count matrix was subsequently produced and differential gene expression was assessed with DESeq2.⁸⁰ Only genes with an absolute fold-change ≥ 2 and an adjusted p-value ≤ 0.05 when contrasting to the corresponding reference samples were defined as differentially expressed.

Hierarchical clustering of flow cytometry data

Unsupervised hierarchical clustering of flow cytometry data was performed using average (UPGMA) clustering method with Euclidean distances as the distance metric. Heatmaps were produced using `heatmap` R package (refers to [Figure 5A](#)).

Gene set-centered analyses

Gene Set Enrichment Analysis (GSEA) was performed with the `clusterProfiler4` R package⁸⁶ using the maximum likelihood log fold changes computed by DESeq2 as the ranking metric. Gene Set Variation Analysis (GSVA) was performed using the GSVA R package. The Molecular Signatures Database (MSigDB, version 7.2; C2 biocarta and reactome v7.4 gene sets for GSVA) and Gene Ontology Biological Process (source date 2021-02-01, retrieved by `gprofiler` via GO.db library), were used as the main sources for gene-set based analyses. Over-representation analyses (ORA) were performed on significantly up- and down-regulated genes by using the `gprofiler2` R package.

Data visualization

Summary plots included in [Figures 1B, 1C, 2A–2C, S2, S3, S6A, S6B, S6E, and S6F](#) were generated using MAFtools⁷⁷ and `GenVisR`.⁸⁷ Plots included in [Figures 3A and 3D](#) were generated using `ggplot2` and `UpSetR`, respectively. Plots included in [Figure 3E](#) were generated using `Circos`.⁸⁸ Volcano plots in [Figure 4A](#) were generated using `ggplot2`. GSEA plots were generated using `gseaplot` function from `clusterProfiler` R package. Mutational signature plots in [Figure S4](#) were generated using `Mutalisk`. Clonality plots in [Figures S5A and S5B](#) were generated using `SciClone`. Bar plots and violin plots were generated with `GraphPad Prism`. See “Software versions” table below for details.

QUANTIFICATION AND STATISTICAL ANALYSIS

Statistical analyses were performed using the `stats` R package and `GraphPad Prism` software. Summary data are presented as mean \pm standard error of the mean (SEM) (bar plots and dot plots), unless otherwise indicated in the figure legends. Student’s *t* test and ANOVA plus Dunnett’s multiple comparisons tests were applied to continuous normal data; and the equivalent non-parametric Mann-Whitney and Kruskal-Wallis tests to data distributions failing normality tests. p-values were corrected for multiple hypothesis testing using the Benjamini-Hochberg procedure where appropriate. Differences were considered statistically significant at $p \leq 0.05$ or adjusted $p \leq 0.05$.